Progress In Electromagnetics Research B, Vol. 40, 101–140, 2012

A DIRICHLET TO NEUMANN MAP BASED HYBRIDIZATION OF A MODE MATCHING AND OFFSET MOMENT METHOD FOR HORN ANTENNAS ANALYSIS

S. G. Diamantis, A. P. Orfanidis, M. Chryssomallis, and G. A. Kyriacou*

Department of Electrical and Computer Engineering of Democritus, University of Thrace, Xanthi, GR 67100, Greece

Abstract—A hybrid technique for the analysis of pyramidal and conical horn antennas is presented based on an exact vector Dirichlet to Neumann (DtN) mapping mathematical formalism. The transition from the feeding waveguide to the radiating aperture is analyzed by using the mode matching technique (MMT) employing a stepped-waveguide approach. Love's field equivalence principle is employed for the definition of equivalent electric and magnetic current densities at the horn aperture. Explicitly, these currents are located at a plane parallel to the aperture but slightly shifted inwards in order to implement an offset Moment Method for their discretization, which is free of integral singularities. The unbounded area field generated by these sources is enforced to be continuous with the internal mode matching field by strictly following DtN principles. Besides that, this procedure mimics a By-moment approach ensuring the decoupling of the required number of modes from that of the sources discretization degrees of freedom. Finally, the implemented hybrid method is validated against published experimental and numerical results for a number of pyramidal and conical horn antennas including various corrugated geometries.

1. INTRODUCTION

The renewed high interest in horn antennas and especially in the multimode soft or hard horns [1, 2], placed the urgent requirement for fast and robust methodologies capable of accurately estimating both their far, near and internal fields as well as quantities related

Received 17 January 2012, Accepted 24 February 2012, Scheduled 9 April 2012

* Corresponding author: George A. Kyriacou (gkyriac@ee.duth.gr).

to them, like the input impedance. Additionally, the modern trend toward miniaturization and broadbanding is addressed with the design of compact horn antennas [1, 3] making the need for analysis methods accurately accounting for the field scattering at the horn aperture more important. This necessity is justified by their electrically small aperture which intensifies the scattering phenomena. It is toward the development of such a method that the present contribution is directed. A lot of works are devoted to horn antenna analysis during the last decades. However, most of them do not take into account the discontinuity between the horn aperture and the free space. For the transition from the small waveguide cross section to the larger radiating aperture a stepped waveguide approach can be used. This model is analyzed by employing the mode matching technique (MMT), since its numerical stability is well established. Different approaches for the analysis of the discontinuity between the horn aperture and the free space have been used, [3–7]. These are mainly based on the mode matching to analyze the horn interior and employed moment method to model its aperture. This paper aims at the establishment of a hybrid MMT and an offset moment method technique for the analysis of the horn antenna. The stepped waveguide model along with the MMT for the analysis of the waveguiding part of the horn is employed. The aperture-free space discontinuity is described by an offset moment method. The latter provides a non-vanishing distance between sources and observation-collocation points, leading to a stable numerical code. It is noticed that the number of sources will be made independent from the number of modes required in the field expansion in the last waveguide section. Due to the above the continuity conditions are imposed first in a point matching scheme and then by integrating over the aperture. This procedure strictly follows the mathematical formalism of Dirichlet-to-Neumann map. Adopting this approach makes the present method mathematically and numerically rigorous and this exactly constitutes the major improvement and the original contribution over our previous work [9, 10]. The metallic horn walls are assumed infinitely thin, or equivalently the possibly significant contribution of the current flowing on the outer surface of the walls is omitted herein in order to first establish the above concept. Note, that this approximation constitutes the usual practice in horn antennas with only a few exceptions like Liu et al. [5]. However, accounting for these currents in the present formulation constitutes our next priority. Besides these, the proposed procedure is applicable to any slotted leaky waveguide or any horn geometry, however this work will be focused on horn antennas.

2. FORMULATION

2.1. Mode Matching Analysis of the Horn Interior

Figure 1 illustrates the geometries of typical pyramidal and conical horn antennas. Following the standard MMT approach [8], the horn antenna is approximated by a series of waveguide sections and step junctions (Figure 2(a)). A junction of two waveguides with different cross section is considered in Figure 2. For each junction (see Figure 2(b)), a common axis of symmetry (axis-z) for the

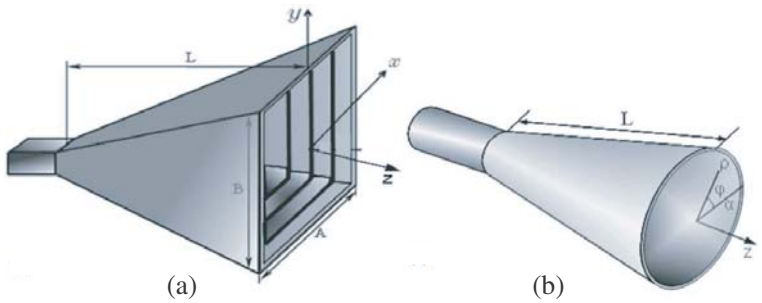

Figure 1. Two typical horn antennas (a) pyramidal and (b) conical horn antenna.

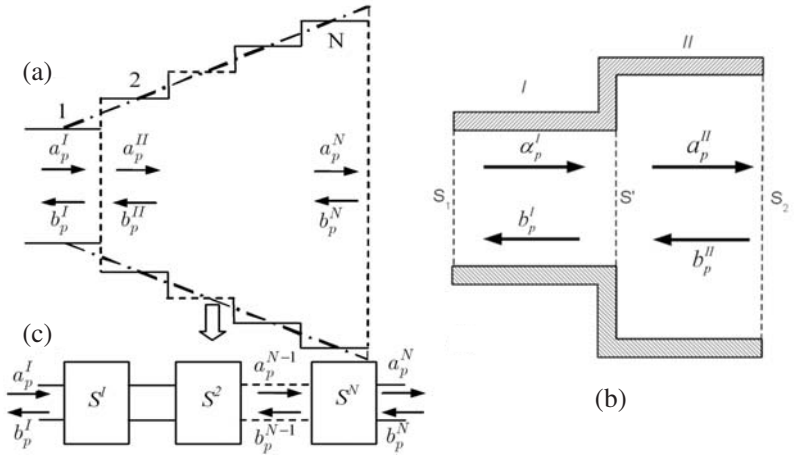

Figure 2. (a) Step waveguide approximation of a horn antenna. (b) Step junction of waveguides with different cross-section and (c) cascaded scattering matrices of discontinuities.

two waveguides with perfectly conducting walls is assumed. The electromagnetic field inside each waveguide is expanded into a modal series, e.g., Marcuvitz [11, p.72]. Modes are numbered in an increasing sequence as they occur. In order for the field expressions to be independent of the excitation magnitude each mode eigenfunction is normalized to the mode power at the junction, as defined by integrating the Poynting vector over the junction surface. Note that for a propagating mode this quantity is real and it represents the power flowing through the junction. In contrary for an evanescent mode this quantity is imaginary corresponding to the energy stored around the junction. Hence, after normalization the mode power (P_p) at the junction is given by [12, p.15] as:

$$P_p = \frac{1}{2}\iint\limits_S \left(\mathbf{E}_p \times \mathbf{H}_p^*\right)\cdot d\mathbf{S} = \begin{cases} 1W & \text{for propagating modes} \\ +jW & \text{for evanescent TE modes} \\ -jW & \text{for evanescent TM modes} \end{cases} \quad (1)$$

The normalization coefficient N_p is defined as $N_p = 1/\sqrt{P_p}$ and it can be calculated from [11, p.67, 73, 75] for the rectangular and circular waveguide. In this manner the transverse electromagnetic field in each waveguide section is represented by an infinite sum of its eigenmodes:

$$\mathbf{E_t} = \sum_{p=1}^{\infty} \left[a_p e^{-\gamma_p z} + b_p e^{\gamma_p z}\right] \cdot Y_p^{-1/2} \mathbf{e}_{\mathbf{t},p} \quad (2)$$

$$\mathbf{H_t} = \sum_{p=1}^{\infty} \left[a_p e^{-\gamma_p z} - b_p e^{\gamma_p z}\right] \cdot Y_p^{+1/2} \mathbf{h}_{\mathbf{t},p} \quad (3)$$

where a_p and b_p are the forward and backward traveling wave phasors, $\mathbf{e}_{\mathbf{t},p}$, $\mathbf{h}_{\mathbf{t},p}$ the transverse normalized vector electric and magnetic field eigenfunctions for pth-mode, γ_p the complex propagation constant, and Y_p the characteristic admittance for the pth-mode. A classical mode-matching technique has been employed, as described in [12], which finally yields the generalized scattering parameters (S) that fully characterize the junction. These S-parameters can be expressed in a general form in terms of integrals over the junction aperture which represents the coupling between the smaller section waveguide pth-mode and the larger waveguide qth-mode (Q_{pq}) and vice-versa. According to [12, p.16] these read:

$$[S_{11}]_{pq} = \Big([Q]_{pq}\,[Q]_{pq}^T + [I]\Big)^{-1} \Big([Q]_{pq}\,[Q]_{pq}^T - [I]\Big) \quad (4)$$

$$[S_{12}]_{pq} = 2\Big([Q]_{pq}\,[Q]_{pq}^T + [I]\Big)^{-1} [Q]_{pq} \quad (5)$$

$$[S_{21}]_{pq} = [Q]_{pq}^{T}\left([I] - [S_{11}]_{pq}\right) \tag{6}$$

$$[S_{22}]_{pq} = [I] - [Q]_{pq}^{T}[S_{12}]_{pq} \tag{7}$$

The elements of the coupling $[\mathrm{Q}]_{pq}$ matrices are known as coupling integrals and result from the application of the field conditions at the junction and depend on the particular waveguide type and its shape. These can be expressed in terms of the electric **e** and the magnetic **h** modal eigenfunctions.

$$[Q_{pq}] = \left[Q_{pq}^{e}\right] = \left[Q_{qp}^{m}\right]^{T} \tag{8}$$

$$Q_{qj}^{e} = \iint\limits_{S}\left(\mathbf{e}_{q}^{II} \times \mathbf{h}_{j}^{I,*}\right)\cdot \hat{z}dS, \quad j = 1, 2, \ldots P \tag{9}$$

where S is the common area of the two waveguides at the junction. Since modes can be either TE or TM, the combinations (p, q) in (8) denote coupling between these modes. Integrals of (8) involve trigonometric and Bessel functions for rectangular and circular waveguide sections respectively, with different orders and arguments and they require an increased computational effort, especially for microwave network synthesis purposes. Once the scattering matrices of the discontinuities are known, the overall scattering matrix of the stepped waveguide part $[S^H]$, is obtained by building up a system of equations comprised of a series of cascaded waveguide section — step junction S-parameters as depicted in Figure 2(c).

There are two factors which affect the accuracy of the Mode Matching Technique. The first is the number of steps in which the horn is divided and the second is the number of modes considered in each waveguide section. Namely, the infinite sum of (2), (3) must be truncated to a finite number high enough to ensure convergence. According to [5] the maximum length of the waveguide sections must be limited to less than $\lambda/32$, while the number of modes in each section should be proportional to its transverse dimension. It is noticed that all coupling integrals involved in MMT are evaluated analytically, in our previous work [8] for circular waveguide discontinuities, while these are given in Bornemann's textbook [12, p.38] for the rectangular waveguide discontinuities, yielding fast and efficient computations.

2.2. Horn Aperture Discontinuity

Usually, in most of Mode Matching Techniques the aperture is assumed to be perfectly terminated for all the incident waveguide modes. This approximation causes inaccuracies, especially in the antenna input impedance, which becomes larger when the electrical dimensions of

the aperture are small. To overcome this problem, the aperture discontinuity is characterized as an imperfect junction between the horn and free space while the field outside the horn is assumed to be generated by the aperture equivalent sources.

2.2.1. Field Expansion Outside the Horn

The aperture antenna problem is shown in Figure 3(a), where equivalent sources are defined for the pyramidal and conical horn case. According to Love's equivalence principle, e.g., [13, p.71]: "The field in the unbounded area outside the horn can be determined in terms of equivalent electric ($\mathbf{J_S}$) and magnetic ($\mathbf{M_S}$) current densities located on the aperture surface" (Figure 3(a)). These equivalent sources are defined in terms of the tangential field components as:

$$\mathbf{J_S} = \hat{z} \times \mathbf{H}_\alpha \text{ and } \mathbf{M_S} = -\hat{z} \times \mathbf{E}_\alpha \tag{10}$$

where $\mathbf{E}_\alpha$ and $\mathbf{H}_\alpha$ are the interior to the horn electric and magnetic fields as defined on its the aperture surface-S. According to [13] the equivalent sources can be restricted only on the horn aperture surface-S.

However, the above approach does not take into account the thickness (assumed infinitely thin) of the horn metallic walls, which are much greater than the electromagnetic wave penetration depth ($\delta_s < 1\,\mu$m in the microwave band). A field equivalence scheme taking horn wall thickness into account has been elaborated by Catedra [24]. Following a similar procedure one may arrives at a slightly different equivalent geometries than those presented in Figure 3, which yields

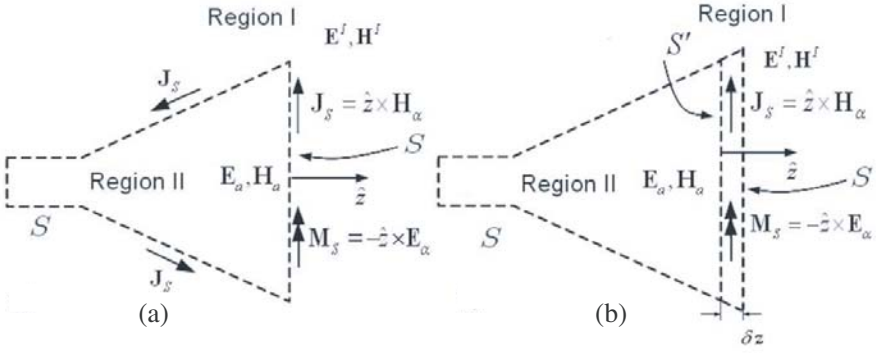

Figure 3. (a) Application of the field equivalence principle for horn antennas and (b) equivalent electric and magnetic sources on the offset surface S'.

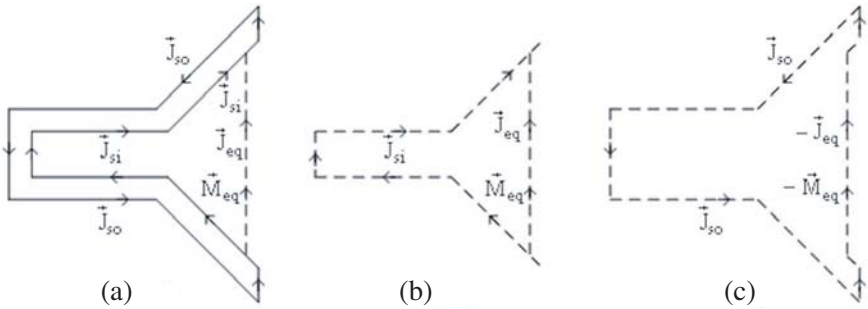

Figure 4. Illustration of the field equivalence principle for a horn antenna when the metallic thickness is considered. (a) Current densities flowing on the walls and equivalent aperture currents. (b) Equivalent internal field model. (c) Equivalent external-unbounded field model.

a somehow larger equivalent surface for the external (unbounded) region fields as presented in Figure 4. Comparing Figures 3 and 4 it is realized that the internal current densities ($\mathbf{J_{Si}}$) as well as the aperture equivalent currents are taken into account in both schemes in the same manner. The former ($\mathbf{J_{Si}}$) is considered within the mode matching internal field formulation, while the equivalent currents ($\mathbf{J_{eq}}$, $\mathbf{M_{eq}}$) are accounted through the field continuity conditions across the aperture following the Dirichlet-to-Neumann map-formalism. Figure 4 clarifies the necessity to include the electric density flowing on the horns outer surface ($\mathbf{J_{So}}$) in the external-unbounded field formulation. This is in accordance with the findings of Liu et al. [5] and these outer current is expect to contribute significantly to the radiation pattern at wide angles and in the rear hemisphere. Although, a highly accurate formulation should take into account the current densities flowing on the horn outside walls, the present effort will be focused on the thin walls assumption. This restriction is necessary in order to reduce the formulation complexity, aiming mainly at the validation of the concept of "exactly enforcing the field continuity conditions at the horn aperture", through the DtN formalism. It is however understood that some inaccuracies in the radiation pattern sidelobes and the back lobe is expected, along with some minor effects on the aperture field distribution and the horn input impedance. Taking these outer surface currents into account it is indeed important and constitutes the next step of this research effort.

The establishment of the present method is based on the field equivalence principle and a small translation of the equivalent sources.

Thus the electromagnetic field in free space region-I (which will be symbolized by the index I) can be described by equivalent electric ($\mathbf{J_S}$) and magnetic ($\mathbf{M_S}$) sources, which are located on a surface S' which is displaced by δz inside to the horn aperture as shown in Figure 3(b) or in Figure 4. Hence, the field $(\mathbf{E}_\alpha, \mathbf{H}_\alpha)$ is established by the mode matching method within the last waveguide section, which defines the equivalent current densities ($\mathbf{J_S}$, $\mathbf{M_S}$) at the aperture. In turn these current densities will be exploited in order to establish the electromagnetic field in the unbounded domain outside the horn. From a first careless point of view, one would consider a general solution of Maxwell equations in the unbounded region, so that it obeys the radiation condition at infinity, and impose the appropriate boundary conditions at the aperture for both $\mathbf{J_S}$ and $\mathbf{M_S}$. This is equivalent to imposing the continuity conditions across the aperture for both the tangential magnetic and electric field between the field expansions inside and outside the horn. While this approach sounds logical and in accordance with the electromagnetism principles, imposing both tangential electric and tangential magnetic field continuity leads to an overdetermined system of equations. A more careful mathematical approach reveals that indeed both field continuity conditions should be enforced, but this should be carried out by strictly following the Dirichlet-to-Neumann map (DtN) mathematical formalism. According to DtN the field solution in the unbounded domain should be first established based on Dirichlet data on the aperture. In turn this solution must be differentiated to establish the DtN map and finally the continuity of the derivatives normal to the aperture (Neumann data) should be impose. The question now is which are the Dirichlet data on the horn aperture? The electric ($\mathbf{J_S}$) or the magnetic ($\mathbf{M_S}$) equivalent current densities or respectively the tangential magnetic ($\mathbf{H}_\alpha$) or the tangential electric field ($\mathbf{E}_\alpha$). One could identify the electric field as Dirichlet data inside the horn, since its walls are assumed perfect electric (PEC), thus imposing Dirichlet boundary conditions on the electric field. Hence the required Dirichlet data on the aperture are comprised of the tangential electric field $\mathbf{E}_\alpha$ or the equivalent magnetic current density ($\mathbf{M_S}$).

In turn the electromagnetic field in the unbounded region outside the horn can be established with the aid of the classical vector electric potential $\mathbf{F}$, e.g., Balanis [14, p.260]:

$$\mathbf{E}^I = -\frac{1}{\varepsilon}\nabla \times \mathbf{F} \tag{11}$$

$$\mathbf{H}^I = -j\omega\mathbf{F} - \nabla\Phi_m \tag{12}$$

where the magnetic scalar potential $\Phi_\mathbf{m}$ and the electric vector

potentials $\mathbf{F}$ are given by [14, p.311]:

$$\mathbf{F}(\mathbf{r}) = \varepsilon \iint_{S'} \mathbf{M_S}(\mathbf{r}')G\left(\mathbf{r},\mathbf{r}'\right) ds' \tag{13}$$

$$\Phi_m(\mathbf{r}) = \frac{1}{\mu} \iint_{S'} \rho_m(\mathbf{r}')G\left(\mathbf{r},\mathbf{r}'\right) ds' \tag{14}$$

The equivalent magnetic charge density is related to the corresponding current density through the charge conservation equation:

$$\rho_m = -\nabla \cdot \mathbf{M_S}/j\omega \tag{15}$$

Finally $G\left(\mathbf{r},\, \mathbf{r}'\right)$ represents the free space Green's function

$$G(\mathbf{r},\mathbf{r}') = e^{-jk|\mathbf{r}-\mathbf{r}'|} \Big/ 4\pi \left|\mathbf{r}-\mathbf{r}'\right| \tag{16}$$

where $\mathbf{r}'$ and $\mathbf{r}$ are the source and observation position vectors designated in Figure 5 and $(k = \omega/c = \omega\sqrt{\mu\varepsilon})$. The magnetic sources surface and the relative location of source points and observation points for pyramidal horn case, are also shown in Figure 5.

2.2.2. Offset Moment Method for the Pyramidal Horn

Expanding the curl of vector potential $\mathbf{F}$, and the gradient of Φ_m, from (11) and (12) in the Cartesian coordinate system, the tangential

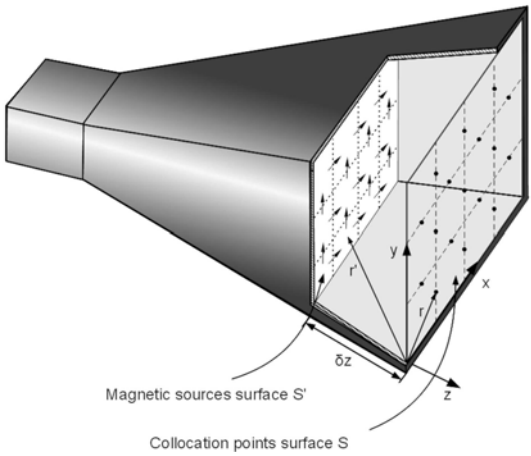

Figure 5. Definition of the magnetic sources surface (S') and collocation point surface (S) for the pyramidal horn antenna.

to the aperture electric and magnetic field components, are given by the relations:

$$E_x^I(x,y,z) = \frac{1}{\varepsilon}\left(\frac{\partial F_y}{\partial z}\right) \tag{17}$$

$$E_y^I(x,y,z) = -\frac{1}{\varepsilon}\left(\frac{\partial F_x}{\partial z}\right) \tag{18}$$

$$H_x^I(x,y,z) = -j\omega F_x - \frac{\partial \Phi_m}{\partial x} \tag{19}$$

$$H_y^I(x,y,z) = -j\omega F_y - \frac{\partial \Phi_m}{\partial y} \tag{20}$$

Using the moment method approach the surface-S' carrying the magnetic sources is discretized into segments in the $-x$ and $-y$ directions respectively, resulting in patches of sizes $\Delta s = \Delta x \Delta y$, as shown in Figure 6. Each component of surface magnetic current density on surface-S', is expanded into a set of overlapping subdomain rooftop triangular basis functions (Figure 7) as follows:

$$M_x\left(x',y'\right) = \sum_{n=1}^{N+1}\sum_{m=1}^{M} M_x^{mn} T_x^{mn}\left(x'-x_m\right) \tag{21}$$

$$M_y\left(x',y'\right) = \sum_{n=1}^{N}\sum_{m=1}^{M+1} M_y^{mn} T_y^{mn}\left(y'-y_n\right) \tag{22}$$

where M_x^{mn}, M_y^{mn} are unknown magnetic current amplitudes and $T_x^{mn}(x',\, y')$, $T_y^{mn}(x',\, y')$ are the triangular subdomain basis functions

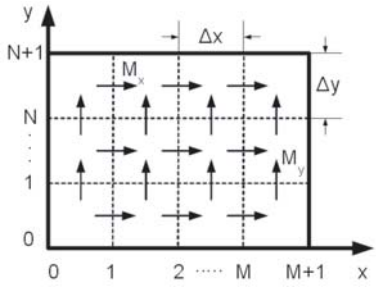

Figure 6. Discretization of magnetic sources surface S' for the inwards offset rectangular aperture surface.

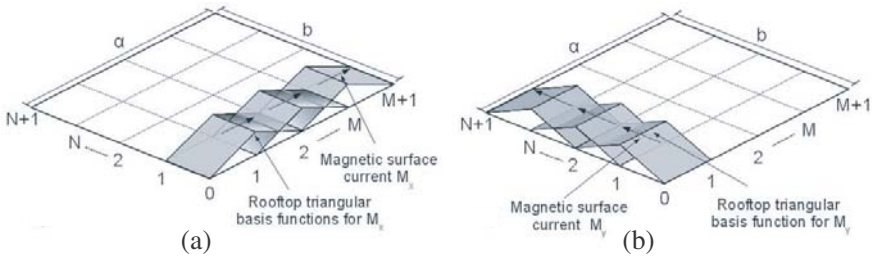

Figure 7. Overlapping subdomain rooftop triangular basis functions (a) for M_x^{mn} expansion and (b) for M_y^{mn} expansion.

which are defined as, [18, p.12]:

$$T_x^{mn}(x',y') = \begin{cases} \dfrac{1-|x'-x_m|/\Delta x}{\Delta y} \text{ for } \begin{matrix} x_{m-1} < x' < x_{m+1} \\ y_{n-1} < y' < y_n \end{matrix} \\ 0 \text{ elsewhere} \end{cases} \tag{23}$$

$$T_y^{mn}\left(x',y'\right) = \begin{cases} \dfrac{1-|y'-y_n|/\Delta y}{\Delta x} \text{ for } \begin{matrix} x_{m-1} < x' < x_m \\ y_{n-1} < y' < y_{n+1} \end{matrix} \\ 0 \text{ elsewhere} \end{cases} \tag{24}$$

Note that, the orientation of the roof top basis functions is selected so that the current density may acquire the proper increase according to the edge singularity, [Collin, "Guided Waves", [21], p.25]. Substituting (21) and (22) into (17)–(20) the tangential electric and magnetic field components read:

$$E_x^I(x,y,z) = -\frac{(z-z')}{4\pi}$$
$$\sum_{n=1}^{N}\sum_{m=1}^{M+1}\int_{x_{m-1}}^{x_m}\int_{y_{n-1}}^{y_{n+1}} M_y^{mn}T_y^{mn}(y'-y_n)\frac{e^{-jkR}}{R^2}\left(jk+\frac{1}{R}\right)dy'dx' \tag{25}$$

$$E_y^I(x,y,z) = \frac{(z-z')}{4\pi}$$
$$\sum_{n=1}^{N+1}\sum_{m=1}^{M}\int_{x_{m-1}}^{x_{m+1}}\int_{y_{n-1}}^{y_n} M_x^{mn}T_x^{mn}\left(x'-x_m\right)\frac{e^{-jkR}}{R^2}\left(jk+\frac{1}{R}\right)dy'dx' \tag{26}$$

$$H_x^I(x,y,z) = -\frac{j\omega\varepsilon}{4\pi}$$
$$\sum_{n=1}^{N+1}\sum_{m=1}^{M}\int_{x_{m-1}}^{x_{m+1}}\int_{y_{n-1}}^{y_n} M_x^{mn}T_x^{mn}\left(x'-x_m\right)\frac{e^{-jkR}}{R}dy'dx' - \frac{\partial\Phi_m}{\partial x} \quad (27)$$

$$H_y^I(x,y,z) = -\frac{j\omega\varepsilon}{4\pi}$$
$$\sum_{n=1}^{N}\sum_{m=1}^{M+1}\int_{x_{m-1}}^{x_m}\int_{y_{n-1}}^{y_{n+1}} M_y^{mn}T_y^{mn}\left(y'-y_n\right)\frac{e^{-jkR}}{R}dy'dx' - \frac{\partial\Phi_m}{\partial y} \quad (28)$$

where $R = \sqrt{(x-x')^2+(y-y')^2+(z-z')^2}$ is the source to observation point distance. Here, primed coordinates denote the source location while unprimed coordinates denote the observation location. In this manner the above integral representations for the vector electric and magnetic potentials are reduced to summations over the discretized sources distributions. Hence, the final expressions for the electric and magnetic field at the aperture surface involve only the unknown weighting factors.

2.2.3. Offset Moment Method for the Conical Horn

For the conical horn, the curl of electric vector potential F, and the gradient of Φ_m, from (11) and (12) are expressed in a circular cylindrical coordinate system. The tangential to the aperture electric

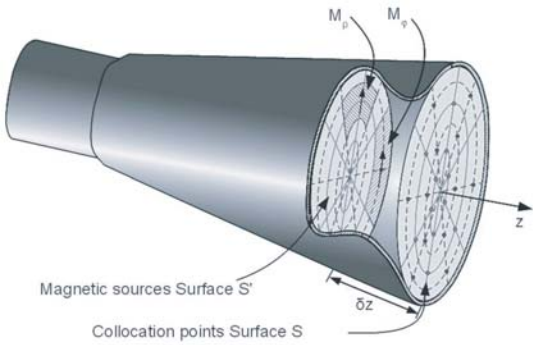

Figure 8. Definition of the magnetic sources surface S' and collocation point surface S for the conical horn.

and magnetic field component, read:

$$E_\rho^I(\rho,\varphi,z) = \frac{1}{\varepsilon}\left(\frac{\partial F_\varphi}{\partial z}\right) \tag{29}$$

$$E_\varphi^I(\rho,\varphi,z) = -\frac{1}{\varepsilon}\left(\frac{\partial F_\rho}{\partial z}\right) \tag{30}$$

$$H_\rho^I(\rho,\varphi,z) = -j\omega F_\rho - \frac{\partial \Phi_m}{\partial \rho} \tag{31}$$

$$H_\varphi^I(\rho,\varphi,z) = -j\omega F_\varphi - \frac{1}{\rho}\frac{\partial \Phi_m}{\partial \varphi} \tag{32}$$

The surface carrying the equivalent magnetic sources is discretized into elementary circular sectors, as shown in Figure 9, with area $\Delta s = \int\limits_{(n-1)\Delta\varphi}^{n\Delta\varphi}\int\limits_{(m-1)\Delta\rho}^{m\Delta\rho} \rho d\rho d\varphi = \Delta\rho^2\Delta\varphi\left(m-\frac{1}{2}\right)$.

Each component, is approximated by a finite number $m \times n$ of pulse basis functions, with unknown amplitudes M_ρ^{mn}, M_φ^{mn}.

$$M_\rho\left(\rho',\phi'\right) = \sum_{n=1}^{N}\sum_{m=1}^{M-1} M_\rho^{mn} \mathrm{P}_\rho^{mn}\left(\rho',\phi'\right) \tag{33}$$

$$M_\phi\left(\rho',\phi'\right) = \sum_{n=1}^{N}\sum_{m=1}^{M} M_\phi^{mn} \mathrm{P}_\phi^{mn}\left(\rho',\phi'\right) \tag{34}$$

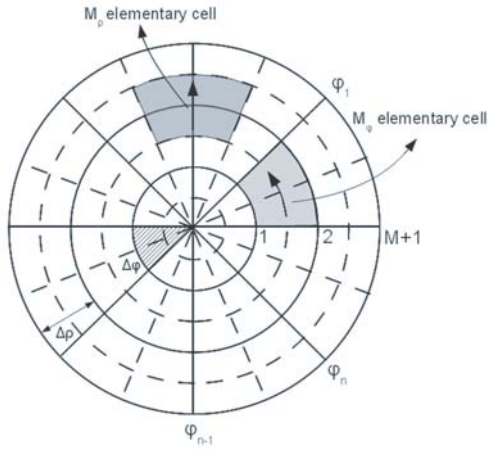

Figure 9. Discretization of the equivalent magnetic current density on a surface S' slightly inside the horn aperture.

where pulse basis functions are defined as:

$$\mathrm{P}_{\rho}^{mn}\left(\rho',\varphi'\right) = \begin{cases} 1 & \text{for } \left(m-\dfrac{1}{2}\right)\Delta\rho \le \rho' \le \left(m+\dfrac{1}{2}\right)\Delta\rho \\ & \quad (n-1)\Delta\varphi \le \varphi' \le n\Delta\varphi \\ 0 & \text{elsewhere} \end{cases} \tag{35}$$

$$\mathrm{P}_{\varphi}^{mn}\left(\rho',\varphi'\right) = \begin{cases} & \quad (m-1)\Delta\rho \le \rho' \le m\Delta\rho \\ 1 & \text{for } \left(n-\dfrac{1}{2}\right)\Delta\varphi \le \varphi' \le \left(n+\dfrac{1}{2}\right)\Delta\varphi \\ 0 & \text{elsewhere} \end{cases} \tag{36}$$

and $\Delta\rho = a/M$, $\Delta\varphi = 2\pi/N$ (a is the aperture radius).

Substituting (33) and (34) in (29)–(32), the tangential to the aperture electric and magnetic field components in the unbounded region I read:

$$E_{\rho}^{I}(\rho,\varphi,z) = -\frac{(z-z')}{4\pi} \sum_{n=1}^{N}\sum_{m=1}^{M} \int_{\left(n-\frac{1}{2}\right)\Delta\varphi}^{\left(n+\frac{1}{2}\right)\Delta\varphi} \int_{(m-1)\Delta\rho}^{m\Delta\rho} M_{\varphi}^{mn} \frac{e^{-jkR}}{R^2}\left(jk+\frac{1}{R}\right)\rho' d\rho' d\varphi' \tag{37}$$

$$E_{\varphi}^{I}(\rho,\varphi,z) = \frac{(z-z')}{4\pi} \sum_{n=1}^{N}\sum_{m=1}^{M-1} \int_{(n-1)\Delta\varphi}^{n\Delta\varphi} \int_{\left(m-\frac{1}{2}\right)\Delta\rho}^{\left(m+\frac{1}{2}\right)\Delta\rho} M_{\rho}^{mn} \frac{e^{-jkR}}{R^2}\left(jk+\frac{1}{R}\right)\rho' d\rho' d\varphi' \tag{38}$$

$$H_{\rho}^{I}(\rho,\varphi,z) = -\frac{j\omega\varepsilon}{4\pi} \sum_{n=1}^{N}\sum_{m=1}^{M-1} \int_{(n-1)\Delta\varphi}^{n\Delta\varphi} \int_{\left(m-\frac{1}{2}\right)\Delta\rho}^{\left(m+\frac{1}{2}\right)\Delta\rho} M_{\rho}^{mn} \frac{e^{-jkR}}{R}\rho' d\rho' d\varphi' - \frac{\partial\Phi_m}{\partial\rho} \tag{39}$$

$$H_{\varphi}^{I}(\rho,\varphi,z) = -\frac{j\omega\varepsilon}{4\pi} \sum_{n=1}^{N}\sum_{m=1}^{M} \int_{\left(n-\frac{1}{2}\right)\Delta\varphi}^{\left(n+\frac{1}{2}\right)\Delta\varphi} \int_{(m-1)\Delta\rho}^{m\Delta\rho} M_{\varphi}^{mn} \frac{e^{-jkR}}{R}\rho' d\rho' d\varphi' - \frac{1}{\rho}\frac{\partial\Phi_m}{\partial\varphi} \tag{40}$$

where $R = \sqrt{\rho^2 + \rho'^2 - 2\rho\rho'\cos(\varphi - \varphi') + (z - z')^2}$.

2.3. Modeling the Aperture Discontinuity-DtN Overview

The aperture discontinuity can be modeled as a generalized scattering matrix by enforcing the field continuity conditions at the aperture. This procedure couples the field expansion in the interior of the horn ($\mathbf{E}^{II,\mathrm{MMT}}$, $\mathbf{H}^{II,\mathrm{MMT}}$) with those of the unbounded exterior region I ($\mathbf{E}^{I,e}$, $\mathbf{H}^{I,e}$), (Figure 10). The continuity conditions should be applied strictly following the Dirichlet-to-Neumann (DtN) mapping mathematical formalism. According to [15, 16], the Dirichlet-to-Neumann map constitutes a nonlocal transparent boundary condition, which has the inherent property to be "exact". The procedure followed for the application of the DtN formulation can be summarized as follows:

(i) An artificial boundary is introduced as to separate the numerical solution domain (horn interior) from the unbounded (free space) area. This surface coincides with the horn walls and its aperture, (Figure 10). Equivalent electric ($\mathbf{J_S}$) and magnetic ($\mathbf{M_S}$) current densities need to be considered only on the horn aperture, according to Love's equivalence principle [13, p.71]. In particular herein the separation surface carrying the equivalent currents is assumed parallel to the horn aperture S but shifted toward the interior of the horn by distance δz, comprising the offset surface S' in Figure 3(b).

(ii) The electromagnetic field inside the horn (region II) established with the aid of the Mode Matching Technique ($\mathbf{E}^{II,\mathrm{MMT}}$, $\mathbf{H}^{II,\mathrm{MMT}}$), where inside each waveguide section a superposition of appropriate number of TE and TM modes is considered. Electric field values can be considered as Dirichlet data, since the horn walls are assumed as perfect electric conductors. In turn, the electric field components tangential to the aperture, define the equivalent magnetic current density ($\mathbf{M_S}$) through (10). Recall again that the equivalent current ($\mathbf{M_S}$) is define along the offset surface S'.

$$\mathbf{M_S} = -\hat{z} \times \mathbf{E}^{II,\mathrm{MMT}}\big|_{S'} \tag{41}$$

(iii) A field solution in the unbounded region-I ($\mathbf{E}^{I}$, $\mathbf{H}^{I}$) is established based on Dirichlet data defined on the artificial separation boundary. Specifically these being the equivalent magnetic current density ($\mathbf{M_S}$) on the horn aperture. This is equivalent to the enforcement of the tangential electric field continuity at the

aperture.

$$\hat{z} \times \mathbf{E}^I\big|_S = \hat{z} \times \mathbf{E}^{II}\big|_S \tag{42}$$

For the field solution in the unbounded region-I the Moment Method (MoM) is applied. But strictly speaking this can be identified as an offset MoM, since the sources ($\mathbf{M_S}$), are located on the offset surface S' while field continuity and the accompanied integration is carried on the aperture surface (S) as shown in Figure 3(b) and specifically in Figures 5, 8.

(iv) Even though one field solution in the unbounded domain-I is established based on the electric field values at the aperture, the offset-MoM of step-3 readily offers both electric ($\mathbf{E}^I$) and magnetic ($\mathbf{H}^I$) fields in region-I. This is equivalent to exploiting the electric field curl equation (differentiating the solution) to obtain the magnetic field. Hence this corresponds to the establishment of a Dirichlet-to-Neumann (DtN) map. In turn the magnetic field values on the aperture represents the corresponding Neumann data and their continuity must be enforced at this step. Respectively, the magnetic field ($\mathbf{H}^I$) components tangential to the horn aperture generates the equivalent surface current ($\mathbf{J_S} = \hat{z} \times \mathbf{H}^I$) which is in turn equal to the tangential magnetic field inside the horn ($\hat{z} \times \mathbf{H}^{II}$) within the last waveguide section.

$$\hat{z} \times \mathbf{H}^I\big|_S = \hat{z} \times \mathbf{H}^{II}\big|_S \tag{43}$$

Recall that adopting the offset approach ($\mathbf{J_S}$) is actually located on the offset surface S'. For this condition to be appropriately applied, Equation (43) must be integrated over the aperture-S. However, in order to exploit the eigenfunction orthogonality properties of the last waveguide section, Equation (43) is successively multiplied by each waveguide eigenfunction and then integrated over S.

The above four step procedure yields an equivalent closed system for the horn antenna, since it provides a generalized scattering matrix for the horn aperture. From a different point of view the DtN approach defines an equivalent surface impedance (or radiation boundary condition) at the horn aperture. The explicit application of the above DtN approach follows next.

2.4. Explicit DtN Approach

2.4.1. Electric Field Continuity (3rd Step)

The tangential electric field components as obtained from MMT (inside the horn) and offset MoM (outside the horn), are point-matched

according to Equation (42) at (n) collocation points, which are located on the aperture surface-S (Figures 5, 8). This condition can be explicitly expressed through (2) and (25), (26) for the pyramidal horn antenna. Likewise, Equations (2) and (37), (38) are used for the conical horn antenna. The resulting expression offers a relation between the modal waveguide coefficients a_p^N, b_p^N and the offset MoM current distribution coefficients (M_x^{mn}, M_y^{mn}) or (M_ρ^{mn}, M_φ^{mn}). But the aim of this step is the establishment of the field in the unbounded region-I, thus to define the MoM current coefficients. Hence, the number of collocation points is selected equal to the MoM degrees of freedom $(n \times n)$ and the continuity equations are enforced on the collocation points. The resulting system of equations is solved to express the weighting factors of the current densities, in terms of the coefficients a_p^N, b_p^N, of the eigenmode expansion used by MMT for the waveguide section just before the aperture. Substituting (2), (25) and (26) in (42) for the rectangular horn case, and (2), (37) and (38) in (42), for conical horn case, after some algebraic manipulations in the matrices form we can write:

$$\left[\begin{bmatrix}[M_{h_1}]\\ [M_{h_2}]\end{bmatrix}\right]_{n\times 1} = \begin{bmatrix}[Q_{h_1}] & \vdots & 0\\ \cdots & \vdots & \cdots\\ 0 & \vdots & [Q_{h_2}]\end{bmatrix}^{-1}_{n\times n} \left[\begin{bmatrix}e^{II}_{h_2,p}\\ e^{II}_{h_1,p}\end{bmatrix}\right]_{n\times P} \left[a_p^{II} + b_p^{II}\right]_{P\times 1} \quad (44)$$

The subscripts $h_1 \rightarrow x, \rho$ and $h_2 \rightarrow y, \varphi$ indicate the different components of magnetic current in different coordinate system (Cartesian and cylindrical for rectangular horn and conical horn respectively). $[M_{h_1}]$, $[M_{h_2}]$ are submatrices with unknown weighting factors and $[Q_{h_1}]$, $[Q_{h_2}]$ are submatrices with ij-elements defined as follows.

For the Pyramidal horn:

$$Q_y^{ij} = \frac{\delta z}{4\pi} \int_{x_{m-1}}^{x_m} \int_{y_{n-1}}^{y_{n+1}} T_y^{mn}\left(y' - y_n\right) \frac{e^{-jkR_{ij}}}{R_{ij}^2} \left(jk + \frac{1}{R_{ij}}\right) dy'dx' \quad (45)$$

$$Q_x^{ij} = -\frac{\delta z}{4\pi} \int_{x_{m-1}}^{x_{m+1}} \int_{y_{n-1}}^{y_n} T_x^{mn}\left(x' - x_m\right) \frac{e^{-jkR_{ij}}}{R_{ij}^2} \left(jk + \frac{1}{R_{ij}}\right) dy'dx' \quad (46)$$

And for the Conical horn:

$$Q_\varphi^{ij} = \frac{\delta z}{4\pi} \int_{(n-1)\Delta\varphi}^{n\Delta\varphi} \int_{(m-1)\Delta\rho}^{m\Delta\rho} \frac{e^{-jkR_{ij}}}{R_{ij}^2} \left(jk + \frac{1}{R_{ij}}\right) \rho' d\rho' d\varphi' \quad (47)$$

$$Q_{\rho}^{ij} = -\frac{\delta z}{4\pi} \int\limits_{(n-\frac{1}{2})\Delta\varphi}^{(n+\frac{1}{2})\Delta\varphi} \int\limits_{(m-\frac{1}{2})\Delta\rho}^{(m+\frac{1}{2})\Delta\rho} \frac{e^{-jkR_{ij}}}{R_{ij}^2} \left(jk + \frac{1}{R_{ij}}\right) \rho' d\rho' d\varphi' \qquad (48)$$

The index j indicates the magnetic cell while the index i indicates the observation point on the aperture and $\delta z = z - z'$ is the distance between the magnetic sources surface-S' and the observation points surface-S.

2.4.2. Magnetic Field Continuity (4th Step)

The electric field in the unbounded region-I is established in the previous step and through its curl the corresponding magnetic field is readily available as a DtN map. Explicitly, the equivalent magnetic current weighting factors obtained through (44) can be exploited in Equations (27), (28) or (39), (40) to yield the magnetic field in the unbounded region-I outside the pyramidal and conical horn respectively. These can be substituted in (43) along with the already available tangential magnetic field inside the horn, from (3), to ensure the tangential magnetic field continuity (continuity of Neumann data or establishment of the equivalent electric current on the aperture). The question now is how to enforce this condition across the entire aperture-S? In order to exploit the orthogonality of the waveguide modes inside the horn, it is preferable to integrate Equation (43) across-S. Hence, the waveguide modes orthogonality properties are exploited to obtain the aperture generalized scattering matrix. Both sides of (43) are multiplied with waveguide mode electric field conjugate eigenfunctions $\mathbf{e}_{\mathbf{j}}^{\mathbf{II},*}(\mathbf{r})$ and integrated over the aperture, the resulting expression reads:

$$\iint\limits_{S} \left(\mathbf{e}_{\mathbf{i}}^{\mathbf{II},*} \times \mathbf{H}_{\mathbf{t}}^{\mathbf{I}}\right) \cdot d\mathbf{S} = \sum_{p=1}^{P} \iint\limits_{S} \left(\mathbf{e}_{\mathbf{i}}^{*,\mathbf{II}} \times \mathbf{h}_{\mathbf{p}}^{\mathbf{II}}\right) \cdot d\mathbf{S} \left[a_p^{II} - b_p^{II}\right], \quad i = 1, 2, \ldots P \qquad (49)$$

Explicitly, the orthogonality property of waveguide modal eigenfunctions $\mathbf{e}_{\mathbf{i}}^{\mathbf{II},*}$, $\mathbf{h}_{\mathbf{p}}^{\mathbf{II}}$ is written as, [19]:

$$\begin{aligned} &\iint\limits_{S} \left(\mathbf{e}_{\mathbf{i}}^{*,\mathbf{II}} \times \mathbf{h}_{\mathbf{p}}^{\mathbf{II}}\right) \cdot d\mathbf{S} = U_p \\ &= \begin{cases} \left.\begin{array}{ll} 2W & \text{for propagating modes} \\ +2jW & \text{for evanescent TE modes} \\ -2jW & \text{for evanescent TM modes} \end{array}\right\} & \text{for } i = p \\ 0 & \text{for } i \neq p \end{cases} \end{aligned} \qquad (50)$$

Hence, the left side of (49) reads:

$$\iint\limits_S \left(\mathbf{e_i^{II,*}} \times \mathbf{H_t^I}\right) \cdot d\mathbf{S} = U_p \left[a_p^{II} - b_p^{II}\right], \quad i = 1, 2, \ldots P \tag{51}$$

$[U_p]$ is a diagonal square matrix with dimensions $P \times P$ determined from (50).

The tangential magnetic field $\mathbf{H_t^I}$ involved in (51) is already expressed as a function of the magnetic current amplitudes (MoM expansion) through Equations (27), (28) for the pyramidal and (39), (40) for the conical horn antenna. Substituting these expressions in (51) and arranging it in matrix form yields:

$$[V]_{P\times n} \begin{bmatrix}[M_{h_1}] \\ [M_{h_2}]\end{bmatrix}_{n\times 1} = [U_p]_{P\times P}\left[a_p^{II} - b_p^{II}\right]_{P\times 1} \tag{52}$$

The ij-th element of matrix $[V]$ represents the coupling integral between the i-th waveguide mode and the j-th magnetic current element, which according to the above algebraic substitutions reads:

$$V_{ij} = \iint\limits_S \left(\mathbf{e_i^{II,*}} \times \mathbf{g_j}\right) \cdot d\mathbf{S} \tag{53}$$

where

$$\mathbf{g_j}(\mathbf{r}) = -j\omega\varepsilon \iint\limits_{S'} G\left(\mathbf{r}, \mathbf{r'_j}\right) ds' - \frac{j}{\omega\mu}\nabla\left(\nabla \cdot \iint\limits_{S'} G\left(\mathbf{r}, \mathbf{r'_j}\right) ds'\right) \tag{54}$$

It should be noticed that, each element of matrix $[V]$ in (53) is a four dimensional integral. In general these types of integrals can be evaluated in closed form, but this requires an excessive algebraic manipulation, which is beyond our present effort. For the pyramidal horn these integrals are reduced into double ones and some characteristic types for both horn types are given in Appendix-B.

2.4.3. Horn Aperture Scattering Matrix

Equation (52) actually represents the tangential magnetic field continuity conditions and involves the equivalent magnetic current amplitudes. However, these are already defined in (44) in terms of the last waveguide section modal coefficients through the tangential electric field continuity conditions. The overall procedure is equivalent to the introduction of a radiation impedance boundary condition at

the horn aperture. Hence, substituting (44) in (52) yields an equivalent closed system in matrix form as:

$$[V]_{P\times n}\begin{bmatrix}[Q_{h_1}] & \vdots & 0\\ \dots & \vdots & \dots\\ 0 & \vdots & [Q_{h_2}]\end{bmatrix}^{-1}_{n\times n}\begin{bmatrix}\begin{bmatrix}e^{II}_{h_2,p}\\ e^{II}_{h_1,p}\end{bmatrix}\end{bmatrix}_{n\times P}\left[a^{II}_p + b^{II}_p\right]_{P\times 1}$$
$$= [U_p]_{P\times P}\left[a^{II}_p - b^{II}_p\right]_{P\times 1} \tag{55}$$

The unknowns of the system in (55) are the amplitudes a^N_p, b^N_p of the forward-incident and backward-reflected waves respectively of each mode at the horn-free space aperture discontinuity. Finally, rearranging (55) one may obtain the generalized aperture reflection matrix $[S^A_{11}]$, which describes the aperture discontinuity. The resulting formulation can be written as follows:

$$\left[b^{II}_p\right] = \left([U_p] + [T_1]\right)^{-1}\left([U_p] - [T_1]\right)\left[a^{II}_p\right] \Rightarrow \tag{56}$$
$$\left[b^{II}_p\right] = \left[S^A_{11}\right]\left[a^{II}_p\right] \tag{57}$$

or

$$\left[S^A_{11}\right] = \left([U_p] + [T_1]\right)^{-1}\left([U_p] - [T_1]\right) \tag{58}$$

where the square matrix $[T_1]$ with dimensions PxP reads:

$$[T_1] = [V]_{P\times n}\begin{bmatrix}[Q_{h_1}] & \vdots & 0\\ \dots & \vdots & \dots\\ 0 & \vdots & [Q_{h_2}]\end{bmatrix}^{-1}_{n\times n}\begin{bmatrix}\begin{bmatrix}e^{II}_{h_2,p}\\ e^{II}_{h_1,p}\end{bmatrix}\end{bmatrix}_{n\times P} \tag{59}$$

2.4.4. Total Horn-aperture Discontinuity Generalized S-matrix

Finally, combining the aperture discontinuity scattering matrix $[S^A_{11}]$ with that of the stepped waveguide scattering matrices $[S^H]$ as depicted in Figure 11, the reflection matrix of the whole horn at its input waveguide section including the aperture reflection is derived as (Figure 11):

$$\left[S^{\text{Total}}_{11}\right] = \left[S^H_{11}\right] + \left[S^H_{12}\right]\left[S^A_{11}\right]\left([I] - \left[S^H_{22}\right]\left[S^A_{11}\right]\right)^{-1}\left[S^H_{21}\right] \tag{60}$$

2.4.5. Horn Antenna Radiated Field

The radiated far zone electric and magnetic field, is identical to that generated by the equivalent surface electric ($\mathbf{J}_s$) and magnetic ($\mathbf{M}_s$)

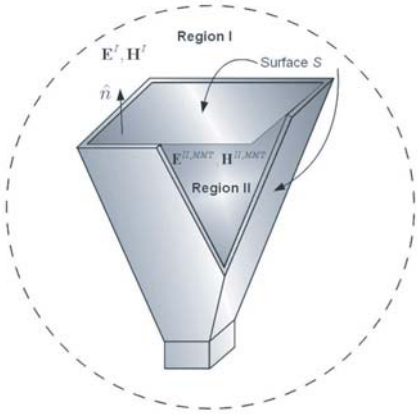

Figure 10. Separation of the horn interior region from the unbounded free space, for DtN application.

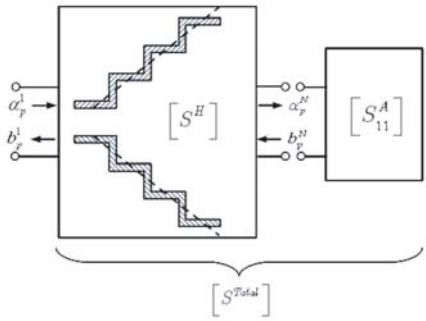

Figure 11. Horn and aperture discontinuity S-matrices combination.

currents defined on the surface S'. Thus the well established procedure which gives the radiation from known electric and magnetic current densities can be readily applied, e.g., Stutzman text book [25, p.375–383]. For completeness the final expressions for the radiated electric field components in spherical coordinates are given below.

$$E_\theta = j\frac{k}{4\pi}\frac{e^{-jkr}}{r}\left(P_x\cos\varphi + P_y\sin\varphi + \eta\cos\theta\left(Q_y\cos\varphi - Q_x\sin\varphi\right)\right) \quad (61)$$

$$E_\varphi = j\frac{k}{4\pi}\frac{e^{-jkr}}{r}\left(\cos\theta\left(P_y\cos\varphi - P_x\sin\varphi\right) - \eta\left(Q_y\sin\varphi + Q_x\cos\varphi\right)\right) \quad (62)$$

where P_x, P_y, Q_x, Q_y are evaluated as follows:

$$P_x = \iint\limits_S E_{\alpha,x} e^{jk(x'\sin\theta\cos\varphi + y'\sin\theta\sin\varphi)} dx'dy' \quad (63)$$

$$P_y = \iint\limits_S E_{\alpha,y} e^{jk(x'\sin\theta\cos\varphi + y'\sin\theta\sin\varphi)} dx'dy' \quad (64)$$

$$Q_x = \iint\limits_S H_{\alpha,x} e^{jk(x'\sin\theta\cos\varphi + y'\sin\theta\sin\varphi)} dx'dy' \quad (65)$$

$$Q_y = \iint\limits_S H_{\alpha,y} e^{jk(x'\sin\theta\cos\varphi + y'\sin\theta\sin\varphi)} dx'dy' \quad (66)$$

$\mathbf{E}_\alpha$, $\mathbf{H}_\alpha$ are the tangential electric and magnetic field on the aperture horn surface respectively, $k = \omega/c$ and $\eta = 120\pi$ *ohms* are the free space wavenumber and its characteristic impedance.

The directivity and the gain of a horn are computed by normalizing the radiated field with the transmitted power and the incident power, respectively. For one incident mode at the input section of the horn, the transmitted power is given by:

$$P_{\text{trms}} = P_{\text{inp}} \left(1 - \sum_{p=1}^{P} |S_{11}(p,1)|^2 \right) \tag{67}$$

where P_{trms} is the transmitted power and P_{inp} is the incident power at the input port of the horn, $S_{11}\,(p,\,1)$ is the reflection coefficient between the p-th mode and the dominant mode at the input port. However, since the normalized eigenfunctions are used, the incident power is equal to unity ($P_{\text{inp}} = 1$), assuming the incident-dominant mode amplitude equal to unity. The directivity and gain patterns are given by:

$$D(\theta,\varphi) = \frac{2\pi}{\eta} \frac{|\mathbf{E}^o(\theta,\varphi)|^2}{P_{\text{trsm}}} \tag{68}$$

$$G(\theta,\varphi) = \frac{2\pi}{\eta} \frac{|\mathbf{E}^o(\theta,\varphi)|^2}{P_{\text{inp}}} \tag{69}$$

where $|\mathbf{E}^o(\theta,\varphi)|^2 = r^2|\mathbf{E}(\theta,\varphi)|^2 = r^2(|E_\theta|^2 + |E_\varphi|^2)$.

3. NUMERICAL RESULTS

To examine the validity of the method five different horn antennas (three pyramidal and two conical) were analyzed. Table 1 presents the dimensions of these pyramidal and conical horn antennas. For MMT analysis each horn antenna was approximated by multiple waveguide step discontinuities with length $\lambda_{\min}/40$ or "40 sections per wavelength" at the maximum frequency of operation. Table 2 shows the parameters for MMT analysis, the number of waveguide step discontinuities approximating each horn antenna, as well as the number of modes required to ensure convergence. Also, Table 2 presents the number of "magnetic cells" considered for the discretization of the equivalent magnetic current on surface S'.

First, the effect of the offset distance δz between the magnetic current surface S' and the collocation points surface S is investigated. Figure 12 presents the relative error for the Voltage Standing Wave Ratio (VSWR) at the input of the horn I, considering a TE_{10} incident

mode (input waveguide operating at its dominant mode) at 11 GHz, as a function of offset distance δz. For this error estimation the measurements given by Bhattacharyya and Rollins [7] are used as reference (exact) data. It is obvious that, when δz tends to zero the VSWR error becomes very large. In this case the collocation surface S tends to coincide with the sources surface (or the method tends to the classical moment method). Thus the increased inaccuracy is due to the approaching of the integration surface toward the Green's function singularities. Namely, the increased inaccuracy is due to the poor handling of the Moment Method singular integrals. For the horn I, when δz is varied from $3\lambda_{\min}/68$ until $\lambda_{\min}/136$ the VSWR error (as shown by the magnified area of Figure 12(b) it oscillates from 0.1% to 3.1%, while it starts to increase again. Hence, the optimum offset distance is $\lambda_{\min}/108 = \lambda_{\max}/140$ which corresponds to locating the sources surface about at the mid-length of the last waveguide section, since its length is set to $\lambda_{\min}/40$.

Table 1. Typical data of the analyzed pyramidal and conical horn antennas.

Type	Input Dimensions a×b in (mm)		Aperture Dimensions $A \times B$ in (mm)		Length in (mm)
	a	b	A	B	L
Horn I	19.05	9.525	34.417	34.417	77.724
Horn II	72.14	34.04	72.14	239.42	346.68
Corrugated Horn	22.86	10.16	90.0	60.0	90.0
	Input Radius in (mm)		Aperture Radius in (mm)		Length in (mm)
Conical Horn I	20.24		55.58		140.0
GPHA [17] Horn	11.60		59.902		286.0

Table 2. Data analysis of rectangular and conical horn antennas.

	Number of waveguide discontinuities	Number of Modes	Number of magnetic cells	Distance δz (mm)
Horn I	145	25	64	$0.2 = \lambda_{\min}/108$
Horn II	154	30	100	$2.0 = \lambda_{\min}/45$
Corrugated Horn	80	90	49	$1.0 = \lambda_{\min}/18$
Conical Horn I	168	60	54	$0.7 = \lambda_{\min}/47$
GPHA [17] Horn	95	80	30	$0.8 = \lambda_{\min}/25$

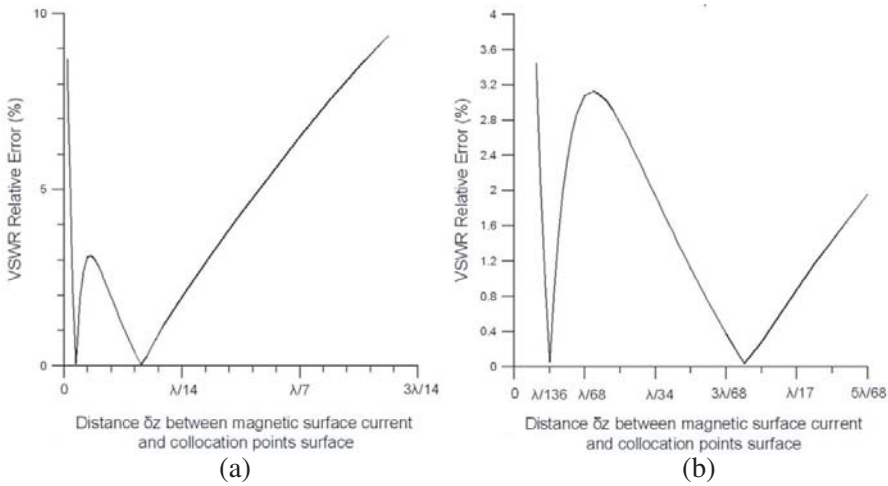

Figure 12. (a) Relative error for the VSWR at the input of the horn antenna I at 11 GHz as a function of distance δz. (b) Enlarged part of a).

The second step studies the convergence of the method versus the number of cells discretizing the surface of equivalent magnetic sources. In Figure 13(a) the convergence rate of the magnitude and phase reflection coefficient at 11 GHz for the horn I, versus the number of cells per square free space wavelength, is presented. The corresponding percent error of magnitude and phase is shown in Figure 13(b) from where it is obvious that at least 64 cells/λ^2 is required for an error less than 2%.

Figure 14 presents the input reflection coefficient of the first horn antenna I, for a TE_{10} incident mode for $\delta z = 0.2\,\text{mm} = \lambda_{\min}/108$ and the number of magnetic surface cells is 144, when the aperture reflection is considered. The line with circular symbols, presents the measurements results from [7] while the solid line presents the calculated input reflection coefficient from the present method. The dashed line presents the reflection coefficient at the input of the antenna when the aperture reflection is ignored. Notice that when the aperture reflection is considered, good agreement between the present method and the measurements is observed. When the aperture reflection is ignored, the measured and computed reflection coefficient at the horn input, do not match.

The normalized input impedance ($\bar{Z}$) at the horn input port is calculated from the reflection coefficient of the incident mode as:

$$\bar{Z} = Z/Z_o = (1 + S_{11})/(1 - S_{11}) \tag{70}$$

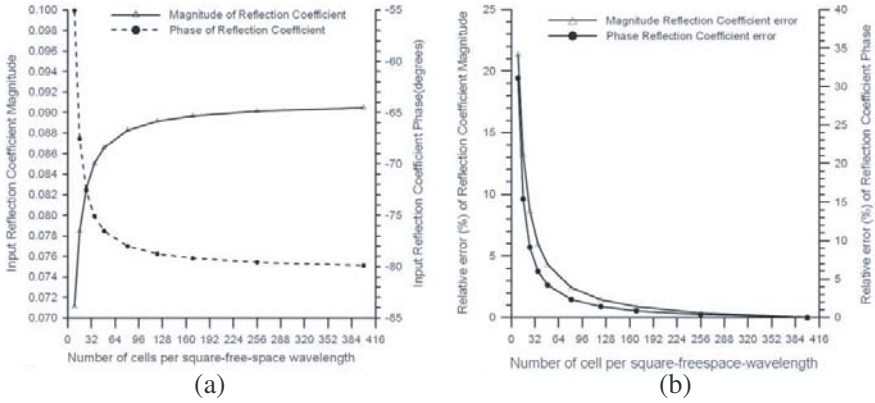

Figure 13. (a) Convergence rate for magnitude and phase of the reflection coefficient for horn I at 11 GHz. (b) Relative error (%) for magnitude and phase of the reflection coefficient for horn I at 11 GHz.

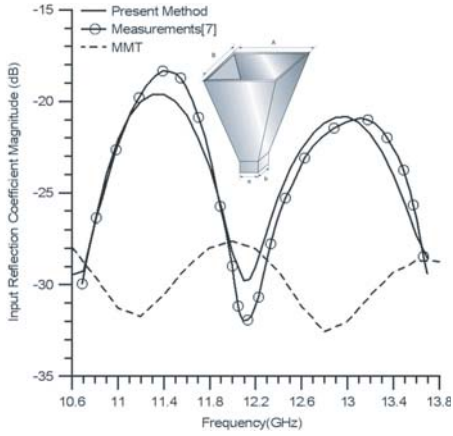

Figure 14. Input reflection coefficient for the horn I.

where Z_o is the corresponding mode characteristic impedance. Figure 15 shows the normalized real and imaginary part of the input impedance for the horn I, when either the aperture effects are accounted or not. Notice that ignoring the aperture effects (MMT) the horn appears fictitiously almost perfectly matched ($\mathrm{Re}\,(Z_{\mathrm{in}}) \simeq Z_o$, $\mathrm{Im}\,(Z_{\mathrm{in}}) \simeq 0$). On the contrary, accounting for the aperture effects a mismatch is revealed where $\mathrm{Re}\,(Z_{\mathrm{in}})$ oscillates around $0.94Z_o$ and $\mathrm{Im}\,(Z_{\mathrm{in}})$ becomes capacitive around $-0.12Z_o$.

Results for the input reflection coefficient of an E-plane sectorial horn in S-band, proposed and analyzed by Encinar [3] using the Hybrid Modal-Spectral Method (HMSM), are compared against those of the present method in the second example. Figure 16 presents the magnitude of reflection coefficient at the input of the horn antenna considering a TE_{10} incident mode or operation of the input waveguide at its dominant mode. The assumed number of modes and the number of magnetic cells as well as the offset δz, are given in Table 2. The dots represent the reflection coefficient from measurements originally given in [4] while the cross symbols represent the reflection coefficient from HMSM. The solid line presents the reflection coefficient when the aperture discontinuity is taken into account by the present method. Good agreement between present method and measurements is observed.

Another four wall corrugated rectangular horn operating in Ku band, is considered in order to validate the method for the E and H-plane radiation pattern. The geometrical characteristics of the corrugated rectangular horn, are presented in Figure 17. The stepped waveguide part was divided in 40 sections per wavelength at the maximum frequency of operation (totally 80 sections), while the number of modes was 90. For the analysis of the aperture discontinuity, the total number of magnetic cells located on the surface S (Figure 6) is 36×24. Figure 18 presents comparisons of radiation patterns of H- and

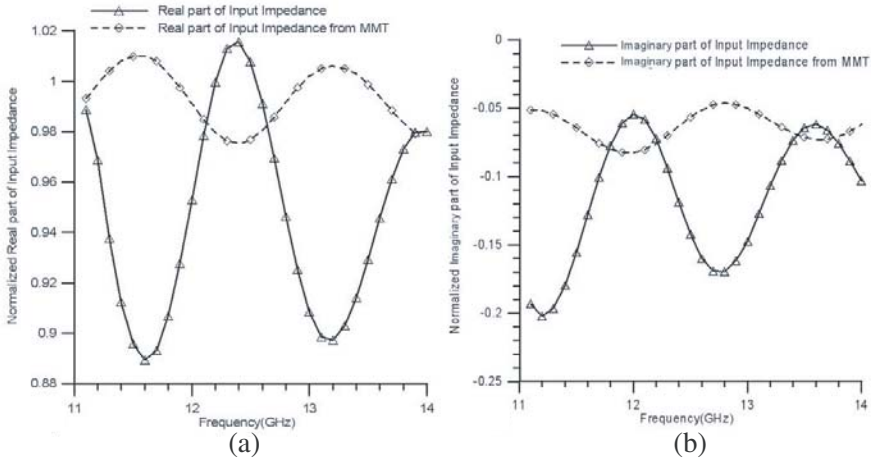

Figure 15. (a) Normalized input impedance Z_{in}/Z_o, (a) real and (b) imaginary parts for the horn I.

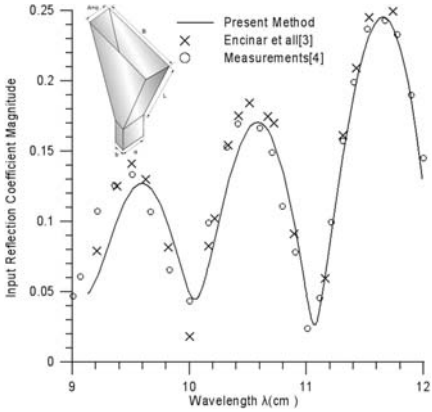

Figure 16. Reflection coefficient at the input of an E-plane sectorial horn.

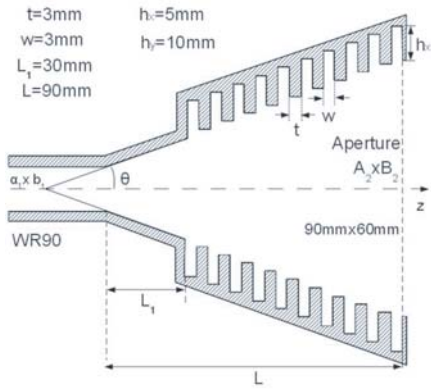

Figure 17. Geometry of corrugated rectangular horn antenna, with its dimensions given in Table 1, [3].

E-plane between the present method and HMSM [3] for the corrugated horn of Figure 17 at 15 GHz. A good agreement between the present method and HMSM [3] is observed in Figure 18 for E and H-plane radiation patterns. Also, Figure 18 shows a comparison of the radiation patterns between the corrugated horn of Figure 17 and a corresponding conventional horn (exactly the same dimensions with horn of Figure 17 but without the internal corrugations). The latter presents a similar main lobe pattern but quite higher sidelobes. The disagreement in the radiated field at angles greater than 60 degrees could be due to the currents flowing on the horn outside surface, however this is not ensured by Figure 18, since both compared methods do not account for these currents.

The input reflection coefficient for the above four wall corrugated rectangular horn, is presented in Figure 19. We can observe that is bellow -16 dB in the whole range from 12 GHz to 17 GHz. Although at 15 GHz the mode TE_{20} is propagated in the input waveguide WR90, its mutual coupling with TE_{10} is negligible. Indeed, the coupling coefficient between them is about 2.68×10^{-6} and 21.27×10^{-6} at 15 GHz and 17 GHz respectively. It is interesting to display the electric field distribution on the corrugated horn aperture and compared it with that of the corresponding conventional horn antenna without corrugations inside. Figure 20(a) presents a three-dimensional plot of the electric field magnitude for the corrugated horn of Figure 17. Figure 20(b) shows the corresponding field for a conventional horn with

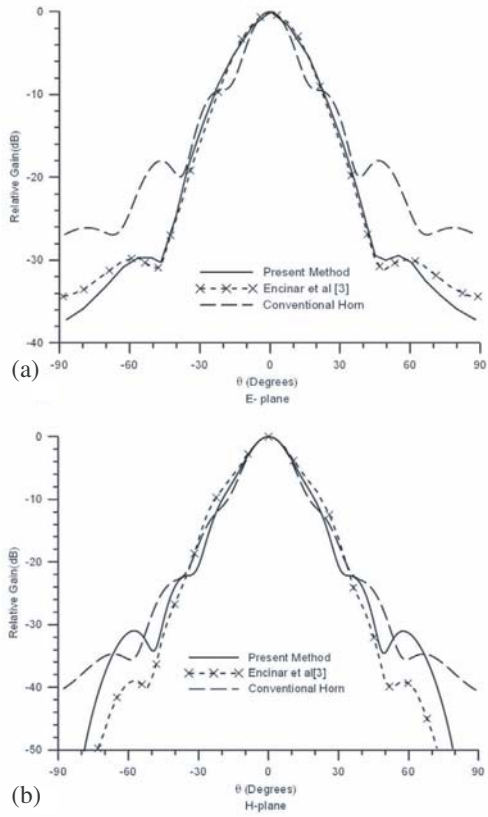

Figure 18. Results of E- and H-plane radiation patterns of the four wall corrugated horn of Figure 17 at 15 GHz, compared against those of Encinar and Rebollar [3]. The patterns calculated for the corresponding conventional (smooth walls) horn are also presented.

exactly same dimensions. Observe that the electric field amplitude (Figure 20(a) is relatively constant over the corrugated horn aperture, while it is abruptly tending to zero around its edges. On the contrary in the case of the conventional horn (Figure 20(b)) tends to zero only along the two of the edges, while it retains a high value at the other two edges. Hence, the corrugated horn is indeed more appropriate for feedings reflectors, avoiding the spillover effects [20].

The conical horn with geometrical characteristics shown in Table 1, was analyzed. The MMT parameters and the number of magnetic cells are given in Table 2. Figure 21 presents the Voltage Standing Wave Ratio (VSWR) at the input port of the conical horn antenna, considering a TE_{11} incident mode for $\delta z = 0.7\,\text{mm} = \lambda_{\min}/47$.

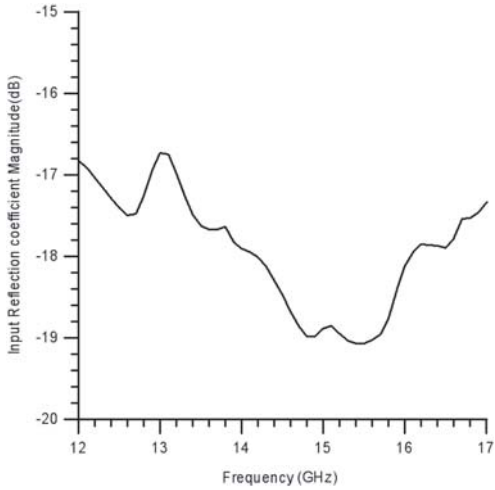

Figure 19. Input reflection coefficient at the input port for the corrugated horn of Figure 17.

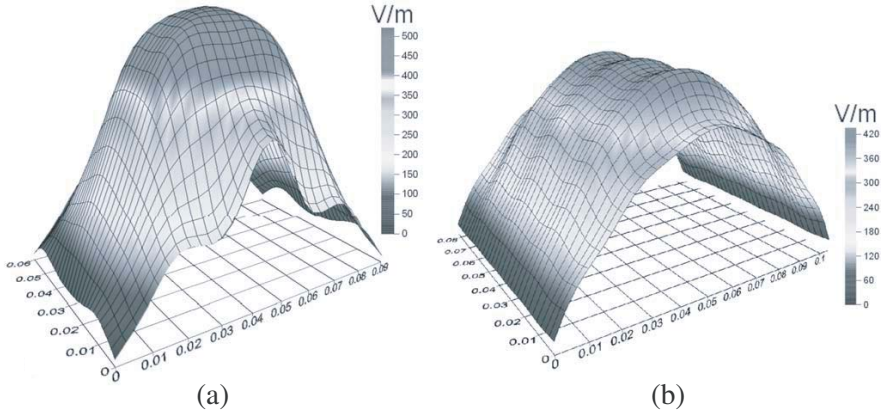

Figure 20. (a) 3D electric field magnitude distribution on the aperture corrugated horn. (b) 3D electric field magnitude distribution on the conventional horn aperture (same horn dimensions without internal corrugations).

The line with rhombus symbols presents the VSWR at the antenna input using commercial software (HFSS v9.1). The solid line refers to the present method while the dashed line presents the VSWR when the aperture reflection is ignored. The importance of the aperture

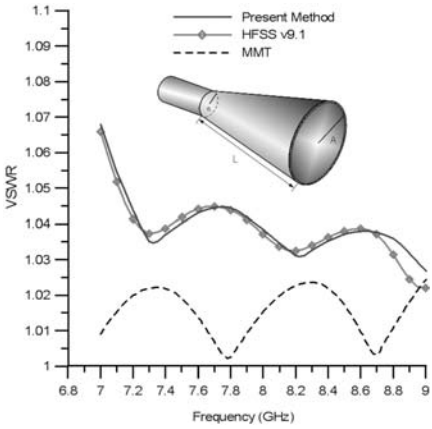

Figure 21. VSWR at the input of the conical horn for TE_{11} mode excitation.

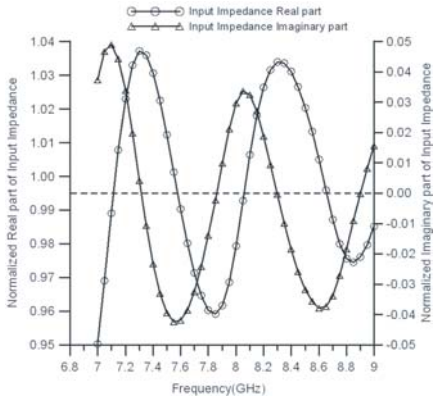

Figure 22. Normalized real and imaginary parts of the input impedance Z_{in}/Z_o, for the conical horn I.

effects is obvious, while a good agreement between the present method and the commercial software results is observed. Figure 22 shows the normalized real and imaginary part of the input impedance for the incident mode. Observe that, when the real part is maximized the imaginary part tends to zero and is very close to the ideal match.

The ultra wide band corrugated Gaussian Profiled Horn Antenna (GPHA) shown in Figure 23 was analyzed. These antenna types have been adopted in many applications due to their excellent radiating properties such as symmetrical patterns, low crosspolar and sidelobes levels [17, 26, 27]. The corresponding waveguide profile which follows the curve for Gaussian equi-amplitude relative surfaces is given by:

$$R(z) = r_{\text{in}}\sqrt{1 + \left(\frac{\lambda z}{\pi a^2 r_{\text{in}}^2}\right)^2} \tag{71}$$

where r_{in} is the inner radius, λ is the wavelength and α is the parameter controlling the aperture angle of the horn. The antenna profile consists of two parts. The design parameters for both horn sections are:

- Design Frequency $f = 11.6\,\text{GHz}$
- Input radius: $r_{\text{in}} = 11.6\,\text{mm}$
- Corrugation parameters: $p = 6\,\text{mm}$, $w = 2\,\text{mm}$, $d = 6.45\,\text{mm}$
- First GPHA section:
  - $\alpha = 2.0$, Length $= 210\,\text{mm}$

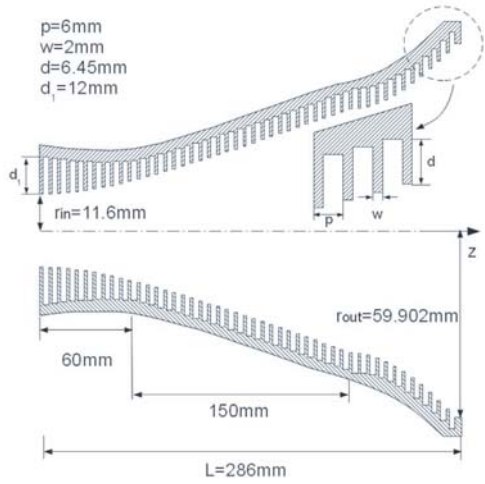

Figure 23. Geometry of corrugated Gaussian profiled horn antenna (GPHA), comprised of cascaded first GPHA section, an impedance transformer and a second GPHA section [17].

  - Impedance transformer: Length = 60 mm, first corrugation depth: $d_1 = 12\,\text{mm}$
- Second GPHA section:
  - Outer radius: $r_{\text{out}} = 59.902\,\text{mm}$, $\alpha = 0.58$, Length = 76 mm.

According to [17], the impedance transformer corrugation depth, decreases linearly from $\lambda/2 = 12\,\text{mm}$ to $\lambda/4 = 6.45\,\text{mm}$ (at 11.6 GHz) as we observe in Figure 23. The parameters for the MMT analysis are shown in Table 2. According to Figure 9 the magnetic sources surface S' is divided into $36 \times 24 = 864$ cells while with this manner the average magnetic cell area is $\lambda_{\text{min}}^2/30$. This choice was made for saving computational resources due to numerical integration in (53). Figure 24 presents the input reflection coefficient of the GPHA horn antenna, considering a TE_{11} incident mode for $\delta z = 0.8\,\text{mm} = \lambda_{\text{min}}/25$. The line with circular symbols, presents the measurements from [17] while the solid line presents the calculated input reflection coefficient from the present method. The input reflection coefficient is bellow $-15\,\text{dB}$ at 11 GHz to 14 GHz frequency band. The results are in good agreement with measurements from [17]. Figure 25 shows the normalized input impedance (real and imaginary part) for the incident mode. We observe that at 11 GHz to 14 GHz frequency band, the imaginary part is very close to zero while the normalized real part is approximately equal to one (perfect match).

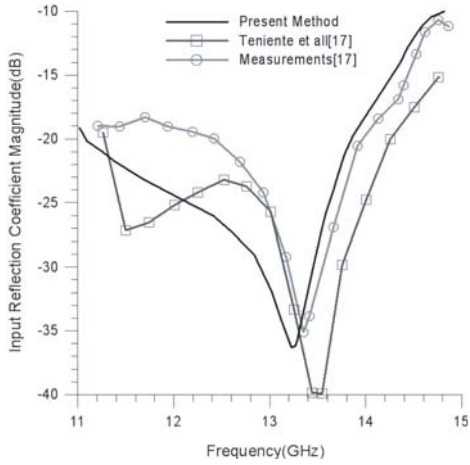

Figure 24. Input reflection coefficient for the GPHA.

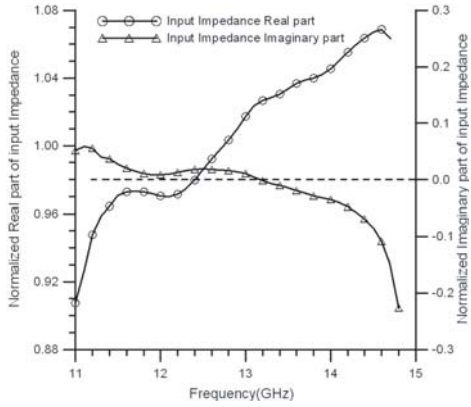

Figure 25. Normalized real and imaginary part of the input impedance, $Z_{\text{in}} \simeq Z_o$ for the GPHA.

Because horn antennas are very often used as gain references in antenna measurements, it is very useful to be able to calculate the horn gain as accurately as possible. It is well known that the gain exhibits an oscillatory behaviour [22, 23].

Results for the gain of a pyramidal horn, proposed and analyzed by Mayhew-Ridgers et al. [23] using the Diffraction Model, are compared against those of the present method. Figure 26 presents the comparison of measured, diffraction model and present method gain values for an X-band pyramidal horn antenna. It is observed that the results from

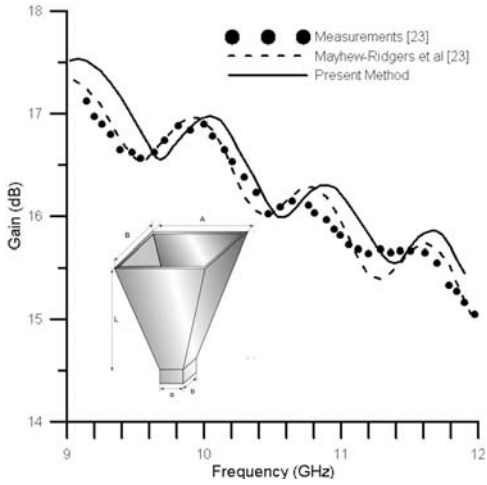

Figure 26. Comparison of an X-band pyramidal horn antenna gain calculated by the present method against measurements and "diffraction model" numerical results [23], (horn dimensions: $A = 194.5\,\text{mm}$, $B = 144.0\,\text{mm}$, $a = 22.46\,\text{mm}$, $b = 10.16\,\text{mm}$, $L = 150.0\,\text{mm}$).

the present method are in good agreement with both measurements and those of the diffraction model, while the gain exhibits indeed an oscillatory behaviour.

Finally, Table 3 compares the present method and the commercial electromagnetic simulator HFSS v9.1 in terms of simulation time and memory requirements for horn I analysis. The present method simulation time is about 30% higher than the HFSS run time, but it should be emphasized that about 60% of the cpu time (12.69 min out of the 21.15 min) of the present method is consumed by the numerical evaluation of integrals given in Appendix B. However, carefully observing the integrals of Appendix B, one may realize that these can be analytically evaluated in closed form. We have indeed evaluated similar integral, even for the cylindrical geometry where these are transformed to Lommel type (involving Bessel functions), in our previous work, e.g., [8]. Certainly, the analytical evaluation of these integrals in closed form will substantially speed up the process making it much faster. However, this task involves extensive analytical manipulations and this is left for a future extension, since herein we focus on the prove of concept. On the other hand the present method's memory requirements are orders of magnitude smaller than those of HFSS.

Table 3. Comparison of the present method against HFSS for horn I operating at a frequency 10 GHz, regarding the simulation time and memory requirements.

	Max Delta S	Lamda Refinement Target	Tetrahedra in Mesh	Run time (min)	Memory (MByte)
HFSS v9.1	0.02	0.333	47247	15.39	973.708
Present Method	–	–	–	21.15	4.664

4. CONCLUSIONS

A Hybrid technique for the analysis of pyramidal and conical horn antennas has been established based on the vector Dirichlet-to-Neumann mapping (DtN) principles. The Mode Matching Technique along with a stepped waveguide model is employed to describe the main part of the horn. This was in turn combined with the offset moment method in order to model the aperture discontinuity between the last waveguide section and the free space. The field continuity conditions across the aperture are enforced by strictly following the DtN mathematical formalism. The procedure is stable and accurate. A good agreement between numerical and commercial software results has been obtained. A future extension of this work includes the study of various types of horn antennas and possibly leaky waveguides. It was indeed observed that neglecting the currents flowing on the horn outside walls causes a small deviation in the radiation pattern at wide angles (greater than 70° from broadside), however we could not identify any related effects on the horn input impedance. Considering these currents in the formulation constitutes our next research task. Besides that, the present method can be readily included within an optimization scheme for the establishment of a horn antenna design tool.

ACKNOWLEDGMENT

This work was financially supported by the Greek Ministry of Education, Lifelong Learning and Religious Affairs through the research project **THALIS** "*Design Techniques for Digitally Controlled RF-Microwave Structures Appropriate for Software Defined — Cognitive Radio* (**RF-EIGEN-SDR**)".

APPENDIX A.

Normalized eigenfunctions for rectangular and cylindrical waveguides: Rectangular Waveguide with internal dimension $\mathrm{a} \times b$.

For TE_{mn} modes:

$$e_x^{\mathrm{TE},n} = j\sqrt{\frac{2\varepsilon_{0m}\varepsilon_{0n}}{\mathrm{a}bk_{c,mn}^2}}\sqrt{\frac{\omega\mu}{|\gamma_{mn}|}}\left(\frac{n\pi}{b}\right)\cos\left(\frac{m\pi x}{\mathrm{a}}\right)\sin\left(\frac{n\pi y}{b}\right)e^{-\gamma_{mn}z} \quad \text{(A1)}$$

$$e_y^{\mathrm{TE},n} = -j\sqrt{\frac{2\varepsilon_{0m}\varepsilon_{0n}}{\mathrm{a}bk_{c,mn}^2}}\sqrt{\frac{\omega\mu}{|\gamma_{mn}|}}\left(\frac{m\pi}{\mathrm{a}}\right)\sin\left(\frac{m\pi x}{\mathrm{a}}\right)\cos\left(\frac{n\pi y}{b}\right)e^{-\gamma_{mn}z} \quad \text{(A2)}$$

$$h_x^{\mathrm{TE},n} = \sqrt{\frac{2\varepsilon_{0m}\varepsilon_{0n}}{\mathrm{a}bk_{c,mn}^2}}\frac{\gamma_{mn}}{\sqrt{|\gamma_{mn}|}}\frac{1}{\sqrt{\omega\mu}}\left(\frac{m\pi}{\mathrm{a}}\right)\sin\left(\frac{m\pi x}{\mathrm{a}}\right)\cos\left(\frac{n\pi y}{b}\right)e^{-\gamma_{mn}z} \quad \text{(A3)}$$

$$h_y^{\mathrm{TE},n} = \sqrt{\frac{2\varepsilon_{0m}\varepsilon_{0n}}{\mathrm{a}bk_{c,mn}^2}}\frac{\gamma_{mn}}{\sqrt{|\gamma_{mn}|}}\frac{1}{\sqrt{\omega\mu}}\left(\frac{n\pi}{b}\right)\cos\left(\frac{m\pi x}{\mathrm{a}}\right)\sin\left(\frac{n\pi y}{b}\right)e^{-\gamma_{mn}z} \quad \text{(A4)}$$

For TM_{mn} modes:

$$e_x^{\mathrm{TM},n} = -\sqrt{\frac{2\varepsilon_{0m}\varepsilon_{0n}}{\mathrm{a}bk_{c,mn}^2}}\sqrt{\frac{1}{\omega\varepsilon\,|\gamma_{mn}|}}\gamma_{mn}\left(\frac{m\pi}{\mathrm{a}}\right)\cos\left(\frac{m\pi x}{\mathrm{a}}\right)\sin\left(\frac{n\pi y}{b}\right)e^{-\gamma_{mn}z} \quad \text{(A5)}$$

$$e_y^{\mathrm{TM},n} = -\sqrt{\frac{2\varepsilon_{0m}\varepsilon_{0n}}{\mathrm{a}bk_{c,mn}^2}}\sqrt{\frac{1}{\omega\varepsilon\,|\gamma_{mn}|}}\gamma_{mn}\left(\frac{n\pi}{b}\right)\sin\left(\frac{m\pi x}{\mathrm{a}}\right)\cos\left(\frac{n\pi y}{b}\right)e^{-\gamma_{mn}z} \quad \text{(A6)}$$

$$h_x^{\mathrm{TM},n} = j\sqrt{\frac{2\varepsilon_{0m}\varepsilon_{0n}}{\mathrm{a}bk_{c,mn}^2}}\sqrt{\frac{\omega\varepsilon}{|\gamma_{mn}|}}\left(\frac{n\pi}{b}\right)\sin\left(\frac{m\pi x}{\mathrm{a}}\right)\cos\left(\frac{n\pi y}{b}\right)e^{-\gamma_{mn}z} \quad \text{(A7)}$$

$$h_y^{\mathrm{TM},n} = -j\sqrt{\frac{2\varepsilon_{0m}\varepsilon_{0n}}{\mathrm{a}bk_{c,mn}^2}}\sqrt{\frac{\omega\varepsilon}{|\gamma_{mn}|}}\left(\frac{m\pi}{\mathrm{a}}\right)\cos\left(\frac{m\pi x}{\mathrm{a}}\right)\sin\left(\frac{n\pi y}{b}\right)e^{-\gamma_{mn}z} \quad \text{(A8)}$$

where $k_{c,mn}^2 = (\frac{m\pi}{\mathrm{a}})^2 + (\frac{n\pi}{b})^2$ the cutoff wave number and propagation constant is:

$$\gamma_{mn} = \begin{cases} j\sqrt{\omega^2\mu\varepsilon - k_{c,mn}^2} & \text{for propagated modes} \\ \sqrt{k_{c,mn}^2 - \omega^2\mu\varepsilon} & \text{for evanescent modes} \end{cases} \quad \text{(A9)}$$

and ε_{0m} is the Neumann factor, which is equal to 1 for $m = 0$ and equal to 2 for $m > 0$.
Cylindrical Waveguide of radius R.

For TE_{nm} modes:

$$e_{\rho}^{\mathrm{TE},n} = -\sqrt{\frac{2}{\pi}}\sqrt{\frac{\omega\mu}{|\gamma_{nm}^{*}|}}\frac{1}{\sqrt{(x_{nm}'^{2}-n^{2})}}\frac{n}{\rho}\frac{J_n(k_c\rho)}{J_n\left(x'_{nm}\right)}e^{-jn\phi}e^{-\gamma z} \quad \text{(A10)}$$

$$e_{\phi}^{\mathrm{TE},n} = j\sqrt{\frac{2}{\pi}}\sqrt{\frac{\omega\mu}{|\gamma_{nm}^{*}|}}\frac{k_c}{\sqrt{(x_{nm}'^{2}-n^{2})}}\frac{J'_n(k_c\rho)}{J_n\left(x'_{nm}\right)}e^{-jn\phi}e^{-\gamma z} \quad \text{(A11)}$$

$$h_{\rho}^{\mathrm{TE},n} = -\sqrt{\frac{2}{\pi}}\frac{\gamma_{nm}}{\sqrt{\omega\mu\,|\gamma_{nm}^{*}|}}\frac{k_c}{\sqrt{(x_{nm}'^{2}-n^{2})}}\frac{J'_n(k_c\rho)}{J_n\left(x'_{nm}\right)}e^{-jn\phi}e^{-\gamma z} \quad \text{(A12)}$$

$$h_{\phi}^{\mathrm{TE},n} = j\sqrt{\frac{2}{\pi}}\sqrt{\frac{\gamma_{nm}}{\omega\mu\,|\gamma_{nm}^{*}|}}\frac{1}{\sqrt{(x_{nm}'^{2}-n^{2})}}\frac{n}{\rho}\frac{J_n(k_c\rho)}{J_n\left(x'_{nm}\right)}e^{-jn\phi}e^{-\gamma z} \quad \text{(A13)}$$

For TM_{nm} modes:

$$e_{\rho}^{\mathrm{TM},n} = \frac{-\gamma_{nm}}{\sqrt{|\gamma_{nm}|\,\omega\varepsilon}}\sqrt{\frac{2}{\pi}}\frac{J'_n(k_c\rho)}{RJ'_n(x_{nm})}e^{-jn\phi}e^{-\gamma z} \quad \text{(A14)}$$

$$e_{\phi}^{\mathrm{TM},n} = \frac{j\gamma_{nm}}{\sqrt{|\gamma_{nm}|\,\omega\varepsilon}}\sqrt{\frac{2}{\pi}}\frac{n}{\rho}\frac{J_n(k_c\rho)}{k_cRJ'_n\left(x_{nm}\right)}e^{-jn\phi}e^{-\gamma z} \quad \text{(A15)}$$

$$h_{\rho}^{\mathrm{TM},n} = \frac{\sqrt{\omega\varepsilon}}{\sqrt{|\gamma_{nm}|}}\sqrt{\frac{2}{\pi}}\frac{n}{\rho}\frac{J_n(k_c\rho)}{k_cRJ'_n\left(x_{nm}\right)}e^{-jn\phi}e^{-\gamma z} \quad \text{(A16)}$$

$$h_{\phi}^{\mathrm{TM},n} = \frac{-j\sqrt{\omega\varepsilon}}{\sqrt{|\gamma_{nm}|}}\sqrt{\frac{2}{\pi}}\frac{J'_n(k_c\rho)}{RJ'_n\left(x_{nm}\right)}e^{-jn\phi}e^{-\gamma z} \quad \text{(A17)}$$

where $k_c^{\mathrm{TE}} = \frac{x'_{nm}}{R}$, $m \in N^{*}$, $k_c^{\mathrm{TM}} = \frac{x_{nm}}{R}$, $m \in N^{*}$, x_{nm} and x'_{nm} are the mth zeros of the nth order Bessel function $J_n(x)$ and Bessel function derivative $J'_n(x)$, respectively and ε, μ relative permittivity and permeability of vacuum respectively. Also, γ is given by (A9).

APPENDIX B.

Indicative coupling integrals at the horn aperture.

Pyramidal Horn:

$$\int_0^b\int_0^a\int_{x_{m-1}}^{x_m}\int_{y_{n-1}}^{y_n}\frac{e^{-jkR}}{R}\frac{\partial}{\partial x}e_y^{w*}(x,y)dy'dx'dxdy \quad \text{(B1)}$$

$$\int_0^b \int_0^{\mathrm{a}} \int_{x_{m-1}}^{x_m} \int_{y_{n-1}}^{y_n} \frac{e^{-jkR}}{R} \frac{\partial}{\partial y} e_x^{w*}(x,y) dy' dx' dx dy \tag{B2}$$

$$\int_0^b \int_0^{\mathrm{a}} \int_{x_{m-1}}^{x_{m+1}} \int_{y_{n-1}}^{y_n} e_y^{w*} T_x^{mn}\left(x' - x_m\right) \frac{e^{-jkR}}{R} dy' dx' dx dy \tag{B3}$$

where $R = \sqrt{(x-x')^2 + (y-y')^2 + (z-z')^2}$.

Each of the above four dimensional integrals, using appropriate change of variable are reduced into a sum of double integrals. For example, the integral in (B1) is simplified to:

$$\int_0^b \int_0^{\mathrm{a}} \int_0^{x_1} \int_0^{y_1} \cos\left(\frac{m\pi x}{\mathrm{a}}\right) \cos\left(\frac{n\pi y}{b}\right) \frac{e^{-jkR}}{R} dy' dx' dx dy =$$

$$\frac{\mathrm{a}b}{mn\pi^2} \left\{ \int_{-x_1}^0 \sin\left(\frac{m\pi(x_1+u)}{\mathrm{a}}\right) \left[\int_{-y_1}^0 \sin\left(\frac{n\pi(y_1+v)}{b}\right) f(u,v) dv \right] du \right.$$

$$+ \int_{-x_1}^0 \sin\left(\frac{m\pi(x_1+u)}{\mathrm{a}}\right) \left[\int_0^{b-y_1} \left(\sin\left(\frac{m\pi(y_1+v)}{\mathrm{a}}\right) - \sin\left(\frac{n\pi}{b}v\right) \right) f(u,v) dv \right] du$$

$$+ \int_{-x_1}^0 \sin\left(\frac{m\pi(x_1+u)}{\mathrm{a}}\right) \left[\int_{b-y_1}^{b_1} (-1) \sin\left(\frac{n\pi}{b}v\right) f(u,v) dv \right] du$$

$$+ \int_0^{\mathrm{a}-x_1} \left[\sin\left(\frac{m\pi(x_1+u)}{\mathrm{a}}\right) - \sin\left(\frac{m\pi}{\mathrm{a}}u\right) \right] \left[\int_{-y_1}^0 \sin\left(\frac{n\pi(y_1+v)}{b}\right) f(u,v) dv \right] du$$

$$+ \int_0^{\mathrm{a}-x_1} \left[\sin\left(\frac{m\pi(x_1+u)}{\mathrm{a}}\right) - \sin\left(\frac{m\pi}{\mathrm{a}}u\right) \right]$$

$$\left[\int_0^{b-y_1} \left[\sin\left(\frac{n\pi(y_1+v)}{b}\right) - \sin\left(\frac{n\pi}{b}v\right) \right] f(u,v) dv \right] du$$

$$\left. + \int_0^{\mathrm{a}-x_1} \left[\sin\left(\frac{m\pi(x_1+u)}{\mathrm{a}}\right) - \sin\left(\frac{m\pi}{\mathrm{a}}u\right) \right] \left[\int_{b-y_1}^b (-1) \sin\left(\frac{n\pi}{b}v\right) f(u,v) dv \right] du \right]$$

$$+\int_{a-x_1}^{a}(-1)\sin\left(\frac{m\pi}{a}u\right)\left[\int_{-y_1}^{0}\sin\left(\frac{n\pi(y_1+v)}{b}\right)f(u,v)dv\right]du$$
$$+\int_{a-x_1}^{a}(-1)\sin\left(\frac{m\pi}{a}u\right)\left[\int_{0}^{b-y_1}\left[\sin\left(\frac{n\pi(y_1+v)}{b}\right)-\sin\left(\frac{n\pi}{b}v\right)\right]f(u,v)dv\right]du$$
$$+\int_{a-x_1}^{a}\sin\left(\frac{m\pi}{a}u\right)\left[\int_{b-y_1}^{b}\sin\left(\frac{n\pi}{b}v\right)f(u,v)dv\right]du\Bigg\} \quad \text{(B4)}$$

where $[f(u,v)=\frac{e^{-jk\sqrt{u^2+v^2+(z-z')^2}}}{\sqrt{u^2+v^2+(z-z')^2}}]$.

Conical Horn:

$$\int_0^a\int_0^{2\pi}\int_{(n-\frac{1}{2})\Delta\varphi}^{(n+\frac{1}{2})\Delta\varphi}\int_{(m-1)\Delta\rho}^{m\Delta\rho}e_\rho^{w*}\frac{e^{-jkR}}{R}\rho'\rho d\rho' d\varphi' d\varphi d\rho \quad \text{(B5)}$$

$$\int_0^a\int_0^{2\pi}\int_{(n-1)\Delta\varphi}^{n\Delta\varphi}\int_{(m-\frac{1}{2})\Delta\rho}^{(m+\frac{1}{2})\Delta\rho}e_\varphi^{w*}\frac{e^{-jkR}}{R}\rho'\rho d\rho' d\varphi' d\varphi d\rho \quad \text{(B6)}$$

where $R=\sqrt{\rho^2+\rho'^2-2\rho\rho'\cos(\varphi-\varphi')+(z-z')^2}$ and subscript w indicates the TE or TM mode.

REFERENCES

1. Deguchi, H., T. Okada, M. Tsuji, and H. Shigesawa, "Multimode horn with optimum gain within circular area," *Electronics and Communications in Japan, Part 1*, Vol. 89, No. 2, 12–20, 2006.
2. Lier, E. and A. Kishk, "A new class of dielectric-loaded hybrid-mode horn antennas with selective gain: Design and analysis by single mode model and method of moments," *IEEE Trans. on Antennas and Propagation*, Vol. 53, No. 1, 125–138, 2005.
3. Encinar, J. A. and J. M. Rebollar, "A hybrid technique for analyzing corrugated and noncorrugated rectangular horns," *IEEE Trans. on Antennas and Propagation*, Vol. 34, No. 8, 961–968, 1986.

4. Jull, E. V., "Reflection from the aperture of a long E-plane sectorial horn," *IEEE Trans. on Antennas and Propagation*, Vol. 20, No. 1, 61–68, 1972.
5. Liu, K., C. A. Balanis, C. R. Birtcher, and G. C. Barber, "Analysis of pyramidal horn antennas using moment methods," *IEEE Trans. on Antennas and Propagation*, Vol. 41, No. 10, 1379–1389, 1993.
6. Wriedt, T., K. H. Wolff, F. Arndt, and U. Tucholke, "Rigorous hybrid field theoretic design of stepped rectangular waveguide mode converters," *IEEE Trans. on Antennas and Propagation*, Vol. 41, No. 37, 780–790, 1989.
7. Bhattacharyya, A. K. and G. Z. Rollins, "Accurate radiation and impedance characteristics of horn antennas-A moment-method model," *IEEE Trans. on Antennas and Propagation*, Vol. 44, No. 4, 523–531, 1996.
8. Orfanidis, A. P., G. A. Kyriacou, and J. N. Sahalos, "A mode matching technique for the study of cylindrical and coaxial waveguide discontinuities based on a closed form coupling integrals," *IEEE Trans. on Microwave Theory and Techniques*, Vol. 48, 880–883, 2000.
9. Diamantis, S. G., A. P. Orfanidis, G. A. Kyriacou, and J. N. Sahalos, "Hybrid mode matching and auxiliary sources technique for horn antenna analysis," *Microwave and Optical Technology Letters*, Vol. 49, No. 3, 734–739, 2007.
10. Diamantis, S. G., A. P. Orfanidis, and G. A. Kyriacou, "Conical horn antennas employing an offset moment method and mode matching technique," *IEEE Trans. on Magnetics*, Vol. 45, No. 3, 1092–1095, 2009.
11. Marcuvitz, N., *Waveguide Handbook*, Peregrinus, Stevenage, UK, 1986.
12. Uher, J., J. Bornemann, and U. Rosenberg, *Waveguide Components for Antenna Feed Systems: Theory and CAD*, Artech House, Norwood, MA, 1993.
13. Collin, R. G. and F. J. Zucker, *Antenna Theory, Part 1*, McGraw-Hill, NY, 1969.
14. Balanis, C. A., *Advance Engineering Electromagnetics*, Wiley, NY, 1989.
15. Keller, J. B. and D. Givoli, "Exact non-reflecting boundary conditions," *J. Comput. Phys.*, Vol. 82, 172–192, 1989.
16. Allilomes, P. C. and G. A. Kyriacou, "A nonlinear finite-element leaky-waveguide solver," *IEEE Trans. on Microwave Theory and Techniques*, Vol. 55, No. 7, 1496–1510, 2007.

17. Teniente, J., R. Gonzalo, and C. del Ro, "Ultra-wide band corrugated profiled horn antenna design," *IEEE Microwave Wireless Components Letters*, Vol. 12, No. 1, 20–21, 2002.
18. Harrington, R. F., *Field Computation by Moment Methods*, IEEE Press, Piscataway, NJ, 1993.
19. Barybin, A. A., "Modal expansions and orthogonal complements in the theory of complex media waveguide excitation by external sources for isotropic, anisotropic, and bianisotropic media," *Progress In Electromagnetics Research*, Vol. 19, 241–300, 1998.
20. Clarricoats, P. J. B. and A. D. Olver, *Corrugated Horns for Microwave Antennas*, IEE Electromagnetics Waves Series 18, Peter Peregrinus, 1984.
21. Collin, R. E., *Field Theory of Guided Waves*, 2nd edition, IEEE Press, 1990.
22. Nye, J. F. and W. Liang, "Theory and measurement of the field of a pyramidal horn," *IEEE Trans. on Antennas Propagation*, Vol. 44, 1488–1498, 1996.
23. Mayhew-Ridgers, G., J. W. Odendaal, and J. Joubert, "Improved diffraction model and numerical validation for horn antenna gain calculations," *International Journal of RF and Microwave Computer-Aided Engineering*, Vol. 19, No. 6, 701–711, 2009.
24. Catedra, M. F., "A comparison between two kinds of equivalent currents to analyze conducting bodies with apertures using moment methods: Application to horns with symmetry of revolution," *IEEE Trans. on Antennas and Propagation*, Vol. 35, No. 7, 782–789, 1987.
25. Stutzman, W., *Antenna Theory and Design*, John Wiley, 1981.
26. Kishk, A. A. and C.-S. Lim, "Comparative analysis between conical and Gaussian profiled horn antennas," *Progress In Electromagnetics Research*, Vol. 38, 147–166, 2002.
27. Zhang, T.-L., Z.-H. Yan, F. Fan, and B. Li, "Design of a Ku-band compact corrugated horn with high Gaussian beam efficiency," *Journal of Electromagnetic Waves and Applications*, Vol. 25, No. 1, 123–129, 2011.